Journal of Materials Chemistry A

REVIEW

View Article Online
View Journal | View Issue

Cite this: J. Mater. Chem. A, 2019, 7, 16571

Redox-active metal–organic frameworks for energy conversion and storage

Joaquín Calbo, [a] Matthias J. Golomb [a] and Aron Walsh *[ab]

Received 5th May 2019
Accepted 17th June 2019

DOI: 10.1039/c9ta04680a

rsc.li/materials-a

Metal–organic frameworks (MOFs) are hybrid solids formed of organic and inorganic building blocks. While the nature of electron addition, removal, and transport is well known in organic and inorganic crystals, the behaviour of hybrid materials is poorly understood in comparison. We review progress over the past 5 years in the study of electroactive MOFs with redox activity promoted by different strategies: (i) redox-active metals; (ii) redox-active organic linkers; (iii) host–guest interactions; and (iv) charge-transfer frameworks. The properties and performance of materials are analysed with respect to emerging application areas including electrochemical energy storage (batteries and supercapacitors) and photo-/electrochemical reactions (solar cells, fuels and electrocatalysis). We further highlight the development of mixed-valence MOFs, which have been found to give rise to unprecedented charge transport in semiconducting and metallic hybrid frameworks.

1. Introduction

Metal–organic frameworks (MOFs) are hybrid materials formed by the coordination of metal ions or clusters (nodes) to organic ligands (struts). MOFs are a relatively new-class of materials that emerged following the seminal work of Yaghi and co-workers reporting in MOF-5 (or IRMOF-1) in 1999.[1] MOF-5 was conceived as a wonder material that had more than three times the internal surface area of the most porous zeolite: one gram of MOF-5 has an internal surface area approximately equal to one regular football field.

Since the discovery of MOF-5, metal–organic frameworks have attracted the attention of coordination chemists and materials scientists as a structurally and chemically versatile hybrid platform. Owing to the modular nature and mild conditions of synthesis, the intrinsic porosity of MOF materials can be systematically modified by judicious selection of molecular building blocks. Moreover, the nature of their large surface area can be fine-tuned by the introduction of a variety of functional sites/groups into the metal ions/clusters, organic linkers, or pore spaces through pre-design or post-synthetic approaches. As a result, MOFs have predominantly found applications in fields such as gas storage, gas separation, and catalysis.[2,3]

Importantly, MOFs can inherit the functions of both metal ions/clusters and organic linkers, so it is possible to engender electronic, magnetic and optical properties in such hybrid scaffolds to develop multifunctional materials.[4–6] As the synthetic methodology reaches a certain level of sophistication, novel applications for MOFs are envisaged, including single-site heterogeneous catalysis and resistive sensing. The field of electrically conducting MOFs has just emerged,[7,8] most notably fostered by redox-activation principles,[9–11] offering a new opportunity for these hybrid materials to be used in fuel cells,[12] supercapacitors,[13] thermoelectrics,[14,15] and electrical switches.[16]

Redox processes related to the loss and gain of electrons are common in nature, and have been employed to build assorted electroactive materials for technological and industrial applications. Traditionally however, MOFs are formed by redox-inactive closed-shell metal centres (*e.g.* d^{10} Zn(II) and d^0 Zr(IV) ions) with inaccessible redox couples, and organic linkers (*e.g.* carboxylates) that hinder electron transfer between the inorganic nodes. Consequently, the vast majority of MOF materials reported up to the last decade are colourless (*i.e.* wide bandgap) insulators. Promoting redox activity in MOFs can be achieved by rational design of both the metal-based nodes and/or the ligand struts that build up the multidimensional framework.[17] The amount of stable oxidation states in transition metals offers a plethora of opportunities to fine-tune the redox-activity in the metal nodes. A rich literature is also present, reporting redox activity in MOFs through ligand engineering. In this regard, both electron-rich and electron-deficient building blocks have been subjected to oxidation and reduction processes, respectively, to foster redox activity through stable radical entities. Finally, the intrinsic porosity of MOFs can be exploited by inserting guest species that promote redox activity or allow tuning the electronic structure of an already redox-active MOF.

In this Review, we tour the strategies used to enable redox activity in hybrid metal–organic frameworks. There are many

[a]Department of Materials, Imperial College London, London SW7 2AZ, UK. E-mail: a.walsh@imperial.ac.uk

[b]Department of Materials Science and Engineering, Yonsei University, Seoul 03722, Korea

excellent reviews of MOFs in general, and in particular of their conductivity, photochemistry, and applications in energy storage.[4,13,18–26] For this reason, we largely restrict our focus to studies reported in the past 5 years, and classify them in terms of the different approaches used for promoting redox activity in MOFs: (i) redox-active metal nodes; (ii) redox-active linkers; (iii) host–guest redox activation; and (iv) charge-transfer frameworks. The materials properties and performance are analysed with respect to emerging application areas.

2. General concepts

2.1. Strategies for chemical modification

There are a number of strategies to realise redox activity in MOFs (Fig. 1).[17] Redox-active metal or ligand entities may be incorporated in the framework in the as-synthesised form. For example, redox-inactive Zr-based nodes can be replaced by electroactive secondary building units (SBUs) containing transition metals with partial d-shell occupation, such as Co(II/III), Cu(I/II), Ni(II/III), *etc.*[27–30] Otherwise, redox-inactive carboxylate ligands can be substituted by a large variety of π-conjugated struts that can promote redox-activity. For instance, the electron-rich TTF unit is one of the most successfully exploited units in building up frameworks with new functionalities that extend across intriguing donor–acceptor charge-transfer phenomena, bandgap modulation, mixed-valency, and tuneable conductivity.[11,31–33]

On the other hand, post-synthetic modification strategies have been employed for redox activation through cation exchange,[34] ligand exchange[35] or incorporation of redox-promoting guest entities.[36] In the latter case, ferrocene is one of the most used units to make MOFs redox-active, leading to the better understanding of the charge-transport mechanisms in these 3D architectures.[37,38] Redox-active guests can be incorporated to the MOF material either by means of covalent grafting (through linkage to the metal node or to the ligand), or by encapsulation exploiting noncovalent interactions.

2.2. Long-range charge transport

While the incorporation of a redox active moiety into a MOF may give rise to redox activity, it will not necessarily promote conductivity associated with the long-range transport of charge, *i.e.* semiconducting or metallic behaviour. The large separation between the electroactive building blocks can be one factor. Poor conjugation pathways arising from the nature of the organic–inorganic bonding, related to the mismatch in energy and/or symmetry in the frontier orbitals of the associated building blocks, also hinder efficient charge-transport processes inside the MOF.

There are two main charge-transport regimes to be considered in MOFs (Fig. 2a): *hopping transport* (spatially localised charge carriers in the form of small polarons) and *band transport* (charge carriers delocalised over 10s to 1000s of atomic centres). In the hopping transport regime, charge carriers (*i.e.* electrons and/or holes) are localised at specific sites with discrete energy levels, and hop between neighbouring sites in a thermally-activated process. This is the mechanism reported in the vast majority of charge-transport studies in MOFs, involving either ligand or node-to-node redox hopping. In the band transport regime, charge carriers are delocalised. However, the band dispersion in MOFs is generally small (*i.e.* the density of states is narrow), the effective masses are large and, thus, the charge mobility is low ($\mu \ll 1$ cm^2 (V^{-1} s^{-1})). The realisation of an effective band transport would yield higher charge mobility and overall conductivity beyond that obtainable from hopping transport, but it is not required for all applications of interest.

Charge-transport pathways can be installed in the lattice of a redox-active MOF by using "through-bond" and "through-space" approaches (Fig. 2b). The through-bond approach aims to promote charge transport *via* favourable spatial and energetic overlap of the metal and ligand orbitals in covalent bonding. The archetypal example of this kind is HKUST-1, where the electron-deficient TCNQ guest interacts coordinatively with vicinal open-site Cu metal nodes to pave a through-bond charge

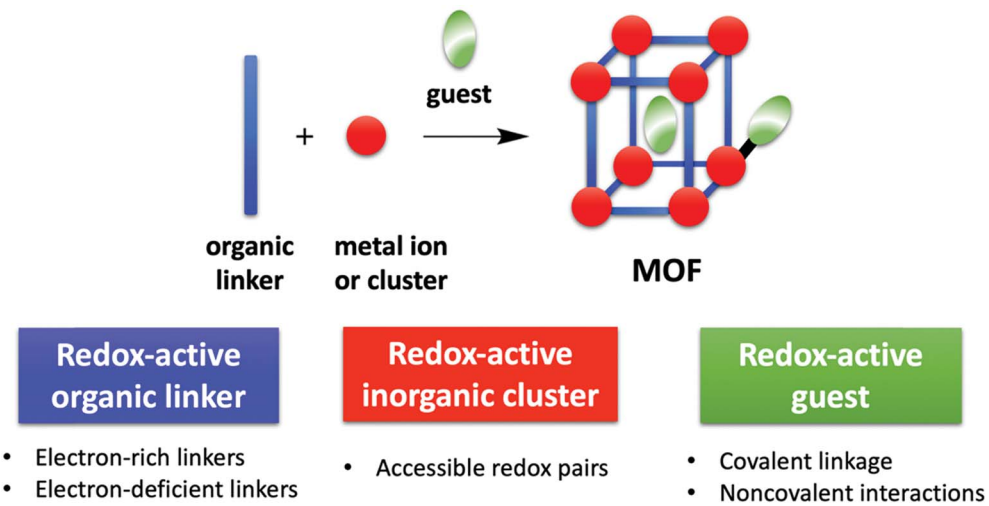

Fig. 1 Types of chemical modifications used to realise redox activity in metal–organic frameworks.

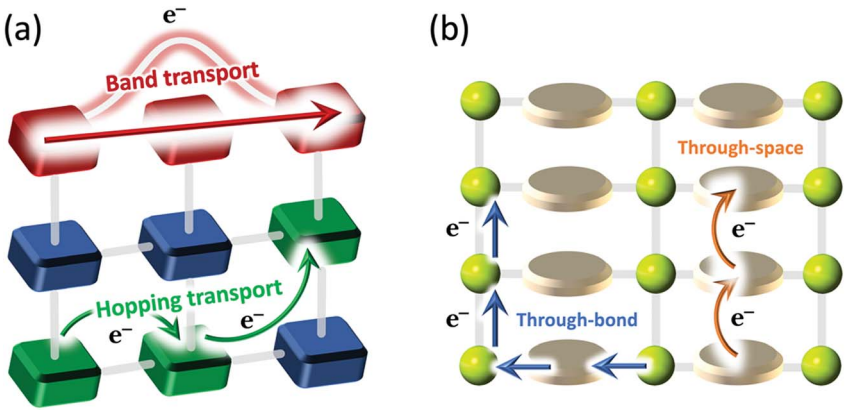

Fig. 2 Schematics of two charge-transport (a) mechanisms and (b) pathways in metal–organic frameworks.

transport pathway.[39] Only recently, the efficient π-conjugation demonstrated in two-dimensional graphene-like MOFs such as $Ni_3(HITP)_2$ and $Ni_3(BHT)_2$ supports electron delocalisation in planar sheets.[40,41] This is translated into an effective overlap between the metal and ligand frontier orbitals, which results in a high conductivity.[42]

On the other hand, through-space approaches enable charge transport *via* non-covalent interactions (such as π–π stacking) between electroactive fragments that are held in place by the metal–ligand scaffold in the MOF, thus circumventing the lack of chemical bonding connection between electroactive building blocks by their close proximity.[33,43] For example, through-space interactions have been observed between the electron donor (TTFTC) and acceptor (DPNI) ligands in $(Zn(DMF))_2(TTFTC)(DPNI)$, where partial charge separation occurs *via* ligand-based radicals formation.[31] When the donor and acceptor moieties are the same entity but only differ in their oxidation state (mixed-valency), a charge-transfer from one moiety to the other can occur, so-called intervalence charge transfer (IVCT). Several mixed-valence MOFs have been synthesized to date, and D'Alessandro *et al.* recently reported the first evidence of an IVCT process occurring *via* a through-space mechanism in a three dimensional network.[44]

2.3. Characterisation of redox activity

Characterisation of redox activity in metal–organic frameworks is just in its infancy, and standard experimental procedures still need to be developed.[17] Solid-state electrochemistry (cyclic and square-wave voltammetry) is the most employed approach to interrogate redox activity, and provide detailed insight into the operating charge-transport mechanism.[45] However, compared to the solution-based electrochemical experiments, solid-state electrochemistry in MOFs face several challenges due to issues related with electrode–MOF and MOF–electrolyte interfaces, and ion diffusion processes.[45,46] In this regard, powder abrasion techniques have proven versatile for adhering solid materials to electrode surfaces,[47,48] and slow-scan cyclic voltammetry may be a key tool for addressing MOFs with slow ion diffusion in the near future.[49]

To assess redox activity in MOFs that require chemical methods for oxidation/reduction, *in situ* solid-state spectroelectrochemical techniques such as UV-Vis-NIR, electron paramagnetic resonance (EPR) and Raman spectroscopies have demonstrated very useful through identification of the spectral signatures of all redox-accessible states of the material.[50,51] Moreover, these techniques have been successfully applied in materials that suffer from degradation during the chemical reduction/oxidation processes,[31,52] and allowed understanding of charge-transport phenomena in MOF-based thin films.[31,44,48] Finally, *in situ* solid-state fluorescence spectroelectrochemical experiments have also been recently applied in the field of redox-active MOFs, showing valuable for assessing the function of materials for optoelectronic device applications.[53,54]

2.4. Applications of computational chemistry

Theory and simulation offers a promising avenue to better understand redox-activity in MOFs.[55] While many applications of MOFs in gas storage and separation can be efficiently described using simple interaction potentials such as Lennard-Jones type forcefields, redox processes require detailed knowledge of the electronic structure. Whereas density functional theory (DFT) was limited in the past to few tens of atoms due to its computational cost, current development in hardware allows high-level full quantum-based calculations of 1000s of atoms in a few days.[56] Quantum-chemistry calculations have already been applied in engineering the bandgap of appealing MOFs for application in photocatalysis and solar energy harvesting,[57] and assisted in the discovery and characterisation of redox-active and conducting frameworks.[58,59]

Charge-transfer phenomena can be accurately described by quantum chemistry methods when the degree of delocalisation is small. For example, the extent of delocalisation in charge-transfer processes can be quantified by application of the Marcus–Hush theory with the help of discrete DFT calculations.[44] Otherwise, when the degree of delocalisation becomes large, with carrier wavefunctions extending beyond a single unit cell, periodic boundary conditions allow treating the hybrid framework in an "infinite" fashion. Record electrical conductivities in iron-based MOFs were demonstrated by means of

periodic DFT calculations to come from high-energy valence electrons of Fe^{2+} and unoccupied mid-gap states originated from Fe^{3+}.[11,30]

High levels of electrical conductivity in 2D MOFs has been recently related with the efficient overlap between linker and metal node frontier orbitals, which leads to a certain dispersion of the band structure.[60] Elucidation of the electronic structure in reciprocal space will give deeper insights into the electronic properties of these novel conducting frameworks.

Finally, the description of the ubiquitous noncovalent (*e.g.* van der Waals) interactions in MOFs can effectively be accounted by the latest advances in low-cost empirically-based DFT-D3 or density-based DFT-NL approximations.[61–63] These approaches have demonstrated of great relevance in predicting selective adsorption,[64] as well as give insight into the mechanism operating in non-trivial redox processes for electrochemical catalysis.[65]

3. Redox-active metal nodes

The number of redox-active MOFs containing transition metals with stable oxidation state pairs is rapidly increasing as new synthetic developments for their realisation become available. In this section, we cover a range of transition metals (with electronic valence configurations from d^0 to d^{10}) in addition to one example of f-electron chemistry with an electroactive lanthanide-based framework (Table 1).

3.1. Titanium

Although the closed-shell Ti(IV) [$3d^0$] species is the most common oxidation state of titanium, redox-activity in Ti-based MOFs can be promoted by reduction of Ti(IV) to Ti(III) [$3d^1$]. Partial occupancy of the d-orbitals in Ti(III) leads to low-energy electronic transitions upon external stimulus. In fact, the unique Ti^{4+}/Ti^{3+} reversible redox conversion upon illumination with UV light together with the excellent thermal/chemical stability and reusability in aqueous and organic systems grant Ti-MOFs huge potential in a wide range of photo-driven catalytic redox reactions.[79]

In 2009, Dan-Hardi *et al.* first reported the reversible photochromic behaviour induced by alcohol adsorption of a highly porous MOF constructed from titanium-oxo-hydroxo clusters and dicarboxylate linkers, so-called MIL-125.[66] The resulting hybrid material exhibited high photon sensitivity, inherent to the titanium-oxo component. UV-visible irradiation promoted the formation of a Ti(IV) MIL-125 with efficient trapping and long-term stability, therefore providing stable coloration. Examination of the electronic and defect structure of MIL-125 demonstrated that chemical reduction of Ti(IV) to Ti(III) can be readily achieved through intrinsic defect formation (oxygen loss) or through extrinsic reductants (*e.g.* H_2).[80] The remarkably low energy for these processes, which is less than those in bulk TiO_2 and below the bandgap energy, allows explaining the facile colour change of this material after UV irradiation.

Further chemical functionalization of the BDC linker in MIL-125 demonstrated the possibility of tuning the optical response of MOFs through rational functionalization of the ligand unit, with the diaminated BDC-$(NH_2)_2$ substitution offering the most significant red shift.[81] Electronic modifications of the ligand aromatic motifs were demonstrated to be localised and directly control the optical properties through modification of the valence band, whereas the conduction band remains centred in the inorganic node (Fig. 3a). The results reported by Hendon *et al.* combining theoretical prediction with experimental validation could be further extended to the larger range of MOFs, enabling predictable bandgap control in property-tailored frameworks (Fig. 3b).[81]

More recently, a novel crystalline material with a two-dimensional structure (MOF-901) has been prepared using a strategy that combines the chemistry of MOFs and covalent-organic frameworks (COFs).[82] Although its redox activity is not extensively exploited yet, the incorporation of Ti(IV) units made MOF-901 useful in the photocatalyzed polymerization of methyl methacrylate.

3.2. Vanadium

Vanadium has four accessible oxidation states ranging from +2 [d^3] to +5 [d^0]. However, only few examples of V-containing MOFs have been reported to date; for a recent review, the

Table 1 Representative MOFs with redox-active metal nodes recently reported in the literature

MOF	Space group	Metal-node oxidation states	Applications	Reference
MIL-125	$I4/mmm$	Ti(III/IV)	Photochromism	66
MFM-300	$I4_122$	V(III/IV)	Selective adsorption; single-site catalysis	67
$Cr_3(BTC)_2\cdot 3H_2O$	$Fm\bar{3}m$	Cr(II/III)	Photochromism	68
$Cr(HFIPBB)\cdot H_2O$	$P2/n$	Cr(II/III)	Photochromism	68
MOF-5	$Fm\bar{3}m$	Mn(II/IV)/Zn(II)	Single-site catalysis	69
MOF-5	$Fm\bar{3}m$	Fe(II/III)/Zn(II)	Single-site catalysis	70
Mn-LMOF	$P\bar{1}$	Mn(II/III)	Supercapacitor	71
Fe_2(DOBDC)	$R\bar{3}$	Fe(II/III)	Selective adsorption; catalysis	72–74
Co-MOF	$C2/c$	Co(II/III)	Electrochemical sensor	75
Co_2Cl_2(BTDD)	$R\bar{3}m$	Co(II/III)	Selective adsorption and storage	27
Ni-CPO-27	$R\bar{3}$	Ni(II/III)	Electrochemical sensor	29
Cu(AQDC)	$P\bar{1}$	Cu(I/II)	Lithium-ion batteries	76
MOF-14	$Im\bar{3}$	Cu(I/II)	Electrochemical sensor; catalysis	77
Ce-ZJU-136	$P\bar{1}$	Ce(III/IV)	Luminescence sensing	78

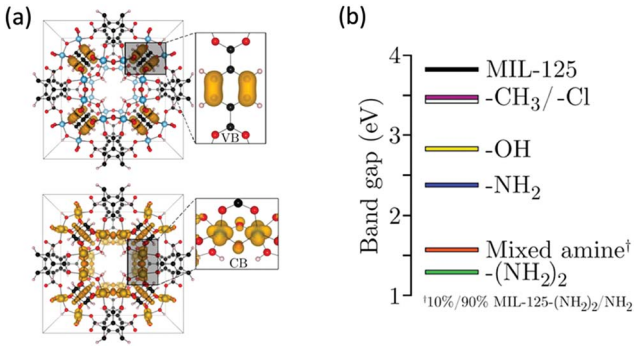

Fig. 3 (a) Frontier electron density for the valence band (VB) and conduction band (CB) of unsubstituted MIL-125 containing Ti(IV)O_6 octahedra. (b) DFT/HSE06-predicted bandgaps of MIL-125 (black) and its analogues containing functionalized BDC linkers. Reprinted with permission from ref. 81. Copyright © 2013 American Chemical Society.

reader is referred to ref. 83. These hybrid materials mostly contain V(III) or V(IV) in the metal nodes.

Recently, Lu *et al.* reported a targeted modification of hydrogen bonding and its effect on guest binding in a redox-active V-MOF.[67] MFM-300 containing V(III) can be oxidized to isostructural MFM-300 containing V(IV), in which deprotonation of the bridging hydroxyl groups occurs. V(III)-MFM-300 showed the second highest CO_2 uptake capacity in metal–organic framework materials at 298 K and 1 bar (6.0 mmol g^{-1}). The CO_2 adsorption process involved hydrogen bonding between the OH group of the host and the O-donor of CO_2, which binds in an end-on manner (Fig. 4a). In contrast, CO_2-loaded V(IV)-MFM-300 showed CO_2 bound side-on to the oxy group and sandwiched between two phenyl groups (Fig. 4b). Oxidation state redox switching in a metal node is therefore an interesting strategy to fine tune the pore environment towards selective adsorption for further exploitation in single-site catalysis. This variation in structure and redox further has led to a notably higher separation selectivity for C_2H_2/CH_4 and C_2H_4/CH_4 in V(III)-MFM-300 than in V(IV)-MFM-300.[84] Owing to the specific host–guest interactions, V(III)-MFM-300 shows a record packing density for adsorbed C_2H_2 at 303 K and 1 bar, demonstrating its potential for use in portable acetylene stores.

3.3. Chromium

Chromium exhibits a range of oxidation states, with +3 [d^3] being the most stable under standard conditions. Due to the high stability of Cr(III) compared to the other oxidation states, reports on the redox-activity of Cr-MOFs are scarce, and MOFs containing *e.g.* Cr(II) are rare. Post-synthetic ion metathesis was successfully employed by Brozek *et al.* to achieve the stoichiometric single oxidation of Cr(II)-MOF-5, as well as other appealing MOF-5 analogues featuring Cr^{3+}, Mn^{2+}, and Fe^{2+} at the metal nodes.[34] The inserted metal ions were coordinated within an unusual all-oxygen trigonal ligand field, and are accessible to both inner- and outer-sphere oxidants: Cr(II)-converts into Cr(III)-substituted MOF-5, while Fe(II)-MOF-5 activates NO to produce an unusual Fe-nitrosyl complex.

More recently, Leszczyński *et al.* reported the synthesis of two redox-active Cr(II)-based MOFs, namely $Cr_3(BTC)_2 \cdot 3H_2O$ and Cr(HFIPBB)$\cdot H_2O$.[68] A dehydration process was demonstrated to be accompanied by a colour change from red to orange, which led to the activated frameworks $Cr_3(BTC)_2$ and Cr(HFIPBB) with the coordinatively unsaturated Cr(II) centres. The authors conducted cyclic voltammetry experiments, demonstrating reversible redox processes associated with multiple oxidation states available for Cr(II/III), III/IV and/or III/V) for the first time in a hybrid framework.

3.4. Manganese

Typical oxidation states of manganese are +2, +3, +4, +6, and +7, though all oxidation states from −3 to +7 have been found.[85] The most stable oxidation state for manganese is Mn(II) [$3d^5$], which is the one commonly found in the Mn-based MOFs reported to date. In a recent work of Stubbs *et al.*,[69] partial substitution of Zn(II) [$3d^{10}$] by Mn(II) in MOF-5 led to a distorted all-oxygen ligand field with a single Mn(II) site forming $MnZn_3O$(terephthalate)$_3$ SBU clusters. The Mn(II) ion at the MOF-5 node engaged in redox chemistry with a variety of oxidants. Intriguingly, an intermediary based on a high-spin Mn(IV)–oxo species was created upon TBSIB treatment. This intermediate was the responsible for a catalysed oxygen atom transfer reactivity to form epoxides from cyclic alkenes with >99% selectivity. MOF secondary building units can therefore serve as competent platforms for accessing terminal high-valent metal–oxo species that subsequently engage in unprecedented single-site catalytic activity.

Recently, Wang *et al.* reported the synthesis of a layered Mn(II)-based MOF, and evaluated its performance as an electrode material for supercapacitors for the first time.[71] The Mn-

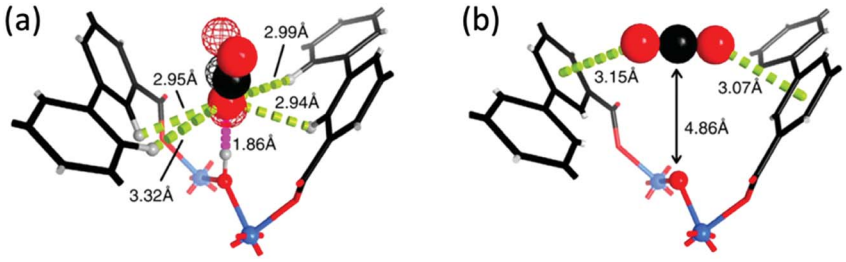

Fig. 4 (a) Interactions of a CO_2 molecule with the hydroxyl and the –CH on phenyl groups in V(III)-MFM-300 through an end-on manner adsorption. (b) 'Sandwiched' binding mode of CO_2 with the phenyl groups in V(IV)-MFM-300. Reprinted with permission from ref. 67. Copyright © 2017 Springer Nature Publishing AG.

LMOF electrode showed a high specific capacitance, a good cycling stability and an improved rate capability. Electrochemical experiments revealed that oxidation/reduction Mn(II/III) processes occur in a reversible manner, whereas charge–discharge profiles demonstrated a pseudocapacitive behaviour originating from the redox reactions taking place at the Mn-LMOF electrode.

3.5. Iron

By far, Fe is the most exploited element for redox-activity in MOFs. Fe is a transition metal with configuration [$4s^2 3d^6$] that leads to stable oxidation states of +2 and +3 to form a [$3d^6$] and a half-filled [$3d^5$] configuration, respectively. The earliest investigations on a redox-active framework material (although not strictly a MOF due to absence of intrinsic porosity) are arguably those on Prussian blue, $Fe_4^{III}[Fe^{II}(CN)_6]_3 \cdot xH_2O$, which has been valued for centuries as a pigment.[86] Despite some ambiguities regarding the exact composition of Fe(II) and Fe(III) in various preparations of Prussian blue, the ability to switch between redox states has been utilised to modulate the conducting, magnetic, gas adsorption, and optical properties of this family of hybrid materials.[87–90]

Fe has been extensively employed as a redox-active centre in the generation of multifunctional MOFs, especially for selective adsorption and catalytic purposes. The large-pore Fe(III) carboxylate Fe-MIL-100 material with a zeo-type architecture reported by Horcajada *et al.* in 2007,[91] showed high activity and selectivity towards Friedel–Crafts benzylation promoted by the presence of Fe(III). The open-site nature of the Fe-based SBUs in MIL-100 was further used for a novel Cu(I) loading method, which led to higher C_3H_6/C_3H_8 selectivity and superior air stability compared to isostructural redox-inactive Cu(I)-loaded Al-MIL-100.[92] Only recently, Brozek *et al.* showed that Fe(II)-MOF-5 promotes nitric oxide disproportionation through a single iron atom to release N_2O.[70] By elucidating how redox reactions occur at the isolated single metal sites in a MOF, mechanistic understanding of similar processes in the same or analogous frameworks is foreseen, giving way for optimizing these materials as ideal platforms for heterogeneous catalysis.

Bloch *et al.* reported in 2011 the selective binding of O_2 over N_2 in the redox-active Fe_2(DOBDC) MOF with open Fe(II) coordination sites.[72] Fe_2(DOBDC) adopts the MOF-74 or CPO-27 structure type, with an $R\bar{3}$ space group and micropores of *ca.* 10 Å. A partial charge transfer from Fe(II) to O_2 was demonstrated at low temperature, and a complete charge transfer to form Fe(III) and O_2^{2-} at room temperature was reported, which was explained in terms of different binding modes. Further studies reported expanded analogues of Fe_2(DOBDC), showing remarkable 3-fold enhancement in alcohol:ketone selectivity for the catalytic oxidation of cyclohexane, and an order of magnitude increase in turnover number, as a result of altering the framework pore diameter and installing nonpolar functional groups near the iron site.[93] Similarly, Xiao *et al.* demonstrated in 2014 that Fe_2(DOBDC) and its Mg-diluted analogue, $Fe_{0.1}Mg_{1.9}$(DOBDC), are able to activate the C–H bonds of ethane and convert it into ethanol and acetaldehyde using nitrous oxide as terminal oxidant.[73] Electronic structure calculations indicated that the active oxidant is likely to be a high-spin Fe(IV)–oxo species. Fe_2(DOBDC) was shown to stabilize iron–superoxo, –peroxo, –hydroxo and –oxo intermediates, which highlights promise for these MOFs both as catalysts and scaffolds for interrogating reactive metal species. Finally, Bloch *et al.* have demonstrated that Fe_2(DOBDC) is able to strongly bind nitric oxide at 298 K as a result of electron transfer from the Fe(II) sites to form Fe(III)–NO^- adducts.[74] The nitric oxide-containing material, $Fe_2(NO)_2$(DOBDC), steadily released bound NO under humid conditions over the course of more than 10 days, demonstrating to be a good candidate for certain biomedical applications. Fe_2(DOBDC) and related MOFs can therefore be seen as appealing platforms for gas adsorption, separation, and as catalysts for the oxidation of hydrocarbons with high selectivity and catalyst stability.

Fe is also intensively employed in the generation of MOFs with mixed-valence phenomena, exploiting partial Fe(II)/Fe(III) composition to reach record conductivities in the field of porous materials.[11,30] The latest and most successful Fe-based mixed-valence MOFs reported so far are discussed separately in Section 6.2.

3.6. Cobalt

Common oxidation states of Co include +2 and +3, giving rise to d-orbital configurations of [$3d^7$] and [$3d^6$], respectively. Cobalt has been incorporated as a redox-active metal in MOFs for electrochemical sensing and selective adsorption. Yang *et al.* synthesized a Co metal–organic framework ($[Co(PBDA)(BP)\cdot 2H_2O]_n$; Co-MOF) under hydrothermal conditions, and then applied the active material for high performance hydrogen peroxide sensing.[75] Importantly, it was found that Co-MOF possessed efficient intrinsic peroxidase-like activity so that it could catalyse H_2O_2 to produce hydroxyl radical, which further oxidizes peroxidase substrate (terephthalic acid) to engender colour. Similarly, a new Co(II/III) mixed-valence MOF has been recently reported by Zhang *et al.*[94] The authors demonstrated for this Co-based MOF containing the redox-active [$Co(II)Co_2(III)(\mu_3$-O)] centres, a high catalytic activity and selectivity towards oxidation of cyclohexene on the allylic position without destroying the adjacent double bond.

Otherwise, Tulchinsky *et al.* have demonstrated that elemental halogens quantitatively oxidize coordinatively unsaturated Co(II) ions in a robust azolate MOF (Co_2Cl_2(BTDD)) to produce stable and safe-to-handle Co(III) materials featuring terminal Co(III)–halogen bonds.[27] The three-dimensional structure of Co_2Cl_2(BTDD) (space group: $R\bar{3}m$) exhibits one-dimensional channels arranged in a honeycomb fashion, with infinite $-(Co-Cl)_n-$ chains coiled into threefold spirals and interconnected by the bis(triazolate) linkers (Fig. 5a). Thermal treatment of the oxidized MOF caused homolytic cleavage of the Co(III)–halogen bonds, reduction to Co(II), and concomitant release of elemental halogens (Fig. 5). The reversible chemical storage and thermal release of elemental halogens occurred with no significant losses of structural integrity. MOFs

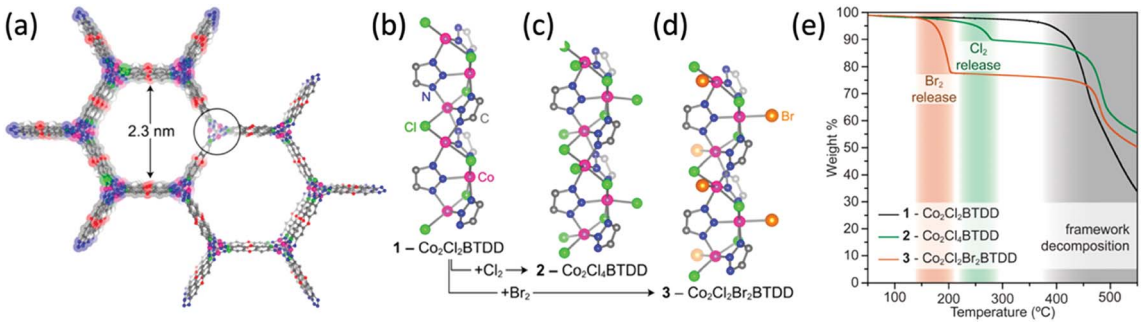

Fig. 5 (a) Structure of the parent Co(II) MOF Co_2Cl_2(BTDD) projected along the *c*-axis. (b–d) SBU structures and local coordination environments of the Co centres in Co_2Cl_2(BTDD), Co_2Cl_4(BTDD) and $Co_2Cl_2Br_2$(BTDD), respectively, as determined by neutron powder diffraction. (e) Thermogravimetric analysis plots; abrupt weight losses below 400 °C correspond to halogen liberation. Reprinted with permission from ref. 27. Copyright © 2017 American Chemical Society.

operating *via* redox mechanism might therefore find utility in the storage and capture of noxious and corrosive gases.

3.7. Nickel

The most recurrent oxidation state of Ni is +2, although compounds of Ni^0, Ni^+, and Ni^{3+} are also well known.[95] Very few examples of the use of Ni(II) with a configuration [$3d^8$] to promote redox activity in MOFs have however been reported. Moon *et al.* reported the synthesis of $[\{Ni(C_{10}H_{26}N_6)\}_3(BPDC)_3]\cdot 2C_5H_5N\cdot 6H_2O$, a porous material that acted as a redox catalyst for the synthesis of silver nanoparticles (*ca.* 3 nm in diameter) at ambient temperature, leading to the generation of Ni(III) species during the nanoparticle formation.[96] More recently, Ni(II)-CPO-27 MOF with high purity, crystallinity, and large surface area was synthesized by Lopa *et al.*[29] A Ni(II)-CPO-27-modified glassy carbon electrode showed excellent redox activity in the alkaline medium due to the formation of Ni(II/III) redox pairs in Ni(II)-CPO-27. A glucose sensor towards its oxidation to gluconolactone was developed, which exhibited wide linear range with high sensitivity and low method detection limit.

Although not directly promoted by redox processes, Ni-based MOFs have flourished in the field of 2D conductive frameworks due to their synthetic modularity, device integration strategies and multifunctional properties.[42] In this regard, Sheberla *et al.* reported in 2014 a new honeycomb 2D-MOF of $Ni_3(HITP)_2$, whose film deposited on quartz substrates consistently gave unprecedented conductivity values of 40 S cm^{-1} at room temperature.[97] This layered MOF (space group: *P*6/*mmm*) presents 1D pore channels of *ca.* 2 nm, with a slipped-parallel AB stacking motif and an interlayer separation of 3.3 Å. Although not fully understood yet, the charge transport mechanism is explained in terms of very efficient 2D pathways between electroactive organic molecules mediated by the Ni metal centres in a planar graphene-like sheet. One year later, Miner *et al.* demonstrated that $Ni_3(HITP)_2$ exhibits oxygen reduction activity competitive with the most active non-platinum group metal electrocatalysts and high stability during extended polarisation.[98]

3.8. Copper

Copper forms a rich variety of compounds, usually with oxidation states +1 [$3d^{10}$] and +2 [$3d^9$].[99] Although several Cu-MOFs have been reported in the literature, redox-activity of Cu-MOFs has been generally overlooked. Zhang *et al.* reported in 2014 a microporous redox-active MOF, namely Cu(AQDC), and utilised it as a cathode active material in Li batteries.[76] With a voltage window of 1.7–4.0 V, both metal Cu_2(acetate)$_4$ paddlewheels and anthraquinone groups in the ligands exhibited reversible redox processes. This MOF constitutes the first example of a porous material showing independent redox activity on both metal cluster nodes and ligand sites.

In 2015, Zhang *et al.* demonstrated the application of a porous Cu(II)-based metal–organic framework with large pore size as a non-enzymatic sensor for the electrochemical determination of hydrogen peroxide and glucose.[77] The Cu-MOF (MOF-14)-modified carbon paste electrode presented a well-behaved redox event due to the electroactive metal centres in the MOF at the physiological pH for further catalytic electroreduction of H_2O_2. One year later, the reduction of Cu(II)-based HKUST-1 was reported by Fu *et al.*[100] The resulting Cu(I)-containing rCu-MOF allowed a series of 'click' reactions with quantitative yield, high activity and facile recyclability. These properties, combined with its ease of synthesis, lack of heavy metal contamination and high structural stability, make the rCu-MOF an attractive catalytic material for industrial applications.

Only recently, Shi *et al.* have reported Cu(I)-based Cu–X–BP (X = iodine) as a high-efficient catalyst in the photocatalytic hydrogen evolution reaction without additional photosensitizers or cocatalysts.[28] Optimization of the activity of luminescent d^{10}-based MOFs through ligand engineering is expected to lead to visible-light-driven hydrogen evolution and their promotion in long-term solar fuels production.

3.9. Cerium

Beyond the 3d and 4d transition metals, f-electron systems are also of great interest to promote redox activity in metal–organic frameworks. Ce [$6s^25d^14f^1$] is the second element in the

lanthanide series. While it often shows the characteristic lanthanide series oxidation state +3 [$4f^1$] as in Ce_2O_3, it also has a stable +4 state [$4f^0$] as in CeO_2. Ce has been recently used as a means of generating redox-active MOFs for catalytic applications. Yue *et al.* successfully realized the cerium-based luminescent Ce-ZJU-136 for the sensitive and selective sensing of ascorbic acid (AA).[78] The redox properties of Ce(IV) in the MOF and the suitable pore size of Ce-ZJU-136 to encapsulate AA for further redox reactions fulfil the requirements for a ''turn-on'' luminescence sensing, particularly useful in biological applications. Unlike the widely explored lanthanide-based (Ln-) MOFs with redox-inactive centres, mainly Tb(III) and Eu(III),[101,102] the realization of this luminescent Ce(IV)-MOF for ''turn-on'' sensing might lead to the discovery of novel sensing materials for environment monitoring and biomedicine.

Otherwise, Smolders *et al.* have presented recently a detailed study of the active site in $[Ce_6O_4(OH)_4]$-based MOFs: Ce-UiO-66 involved in the aerobic oxidation of benzylalcohol and was chosen as a model redox reaction.[103] X-ray absorption spectroscopy data confirmed the reduction of up to one Ce(IV) ion per Ce_6 cluster into Ce(III) cations, while not compromising the structural integrity of the framework. The authors unambiguously demonstrated the involvement of the Ce-based metal node in the catalytic cycle, and gave clues on the importance of TEMPO as a redox mediator to bridge the gap between the one-electron oxidation of the Ce(IV)/Ce(III) couple and the two-electron oxidation of benzylalcohol.

4. Redox-active organic linkers

The versatility of organic linkers that can be used in the growth of multidimensional metal–organic frameworks establishes the source of a tremendous range of possibilities to promote redox activity in such materials. Redox-active MOFs with non-innocent ligands are historically prompted by the inclusion of electroactive organic moieties during the framework synthesis.[45] However, novel post-synthetic procedures confer new avenues to introduce redox-active ligands for the creation of multifunctional frameworks.[104] Moreover, apparently redox-inactive linkers may eventually promote redox activity, as recently reported on a 2D Ni-based hybrid framework, where electron delocalisation was demonstrated critical for accessing key intermediates that become energetically prohibitive for analogous molecular systems.[105] In this section, we describe the latest and most successful attempts in promoting redox-activity through electroactive ligand incorporation (see Fig. 6 for a list of representative struts and Table 2 for a collection of recently reported MOFs with redox-active ligands).

4.1. Naphthalenediimide (NDI)

Owing to their electron deficiency and aromatic nature, as well as their facile functionalization, NDIs have been extensively investigated as n-type semiconductors in organic electronics.[115–117] Because functionalization of the NDI core leads to derivatives that can be easily reduced and absorb light across the visible spectrum,[117] these molecules have been used in MOF-based applications that target optical reading of an input or analyte, such as sensing[118,119] and electro-/photochromism.[17,50,107,120,121]

N,*N*-Dipyridil NDI was incorporated by Mulfort *et al.* as a ligand in a Zn-based MOF to generate $Zn_2(NDC)_2(DPNI)$.[106] The chemical reduction of this 2-fold interpenetrated MOF *via* lithium metal exposure through formation of DPNI radical

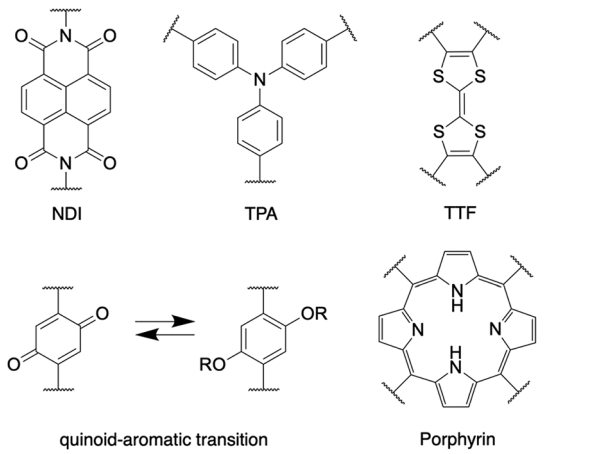

Fig. 6 Representative organic linkers that have been employed in the generation of redox-active MOFs.

Table 2 Comparison of novel MOFs with redox-active ligands

MOF	Space group	Ligand oxidation states	Applications	Ref.
$Zn_2(NDC)_2(DPNI)$	$P2_1$	$(DPNI)^{0/1-}$	Selective adsorption; H_2 storage	106
Zn(NDI-X)	$I4_1/amd^a$	$(NDI\text{-}X)^{0/1-/2-}$	Electrochromic materials	107
$[Mn(TPPA)Cl\cdot 3MeOH\cdot DMF]_n$	$Pbcn$	$(TPPA)^{0/1+}$	Host–guest sensing	53
Cu-TCA	$P2_1/c$	$(TCA)^{3-/2-}$	Lithium-ion batteries	108
$M_2(TTFTB)$	$P6_5$	$(TTFTB)^{4-/3-}$	Electronic devices	33 and 43
MUV-2	$P\bar{6}2m$	$(TTFTB)^{4-/3-}$	Electrochemical sensing	109 and 110
$Mn_2(DOBDC)$	$R\bar{3}$	$(DOBDC)^{4-/2-}$	Redox reactivity and catalysis	111
$[Tl(TCNQX_2)]$	$P2/c$, $P\bar{1}$, $P2_1/c$	$(TCNQX_2)^{0/\delta-}$	High conductivity; electronic devices	112
CoPIZA	$P2_1/n$	Co(I/II/II)	Electrocatalysis	48
Fe-MOF-525	$Pm\bar{3}m$	Fe(0/I)	Electrocatalysis	113
Pt-UiO-67	$Fm\bar{3}m^b$	Pt(II/IV)	Redox catalysis	114

[a] Space group for parent Co(DMDPB). [b] Space group for pristine UiO-67.

anion demonstrated to enhance N_2 sorption due to the mobility of the networks in the solid state. Further studies of this family of NDI-containing MOFs reported by Bae *et al.* demonstrated that strut-centred chemical reduction and cation exchange significantly improves CO_2/CH_4 selectivity through favourable displacement of catenated frameworks and enhances solid–gas desolvated-Li(charge)/CO_2(quadrupole) interactions, respectively. Similar conclusions were reported by Leong *et al.* in Zn(NDC)(DPMBI), with enhanced CO_2/N_2 selectivity in the reduced framework attributed to stronger interactions between CO_2 and the radical DPMBI ligand backbone.[122] Recent work of Tian *et al.* on lithium-ion batteries demonstrated that inclusion of DPNI allows generation of low-dimensional Cd-based frameworks with variable porosity, which leads to a ligand-centred redox reaction during the lithiation–delithiation process.[123]

The incorporation of redox-active linkers also represents one important strategy toward improving the charge-transport properties of MOF materials as well as imparting a response to electrochemical stimuli to obtain colour-tuneable electrochromic materials. This has been exemplified by recent work of Wade *et al.*,[107] which reported the use of NDI ligands to deposit a Zn(NDI-X)-based MOF (X = H, S–C_2H_5, NH–C_2H_5) on a conductive FTO surface to afford electroactive films that exhibit fast and reversible colour switching. Otherwise, the deliberate insertion of redox-active naphthalene diimide ligands into the versatile family of MOF-74 (CPO-27) MOFs gave rise to mesoporous electrochromic frameworks that can be switched from transparent to dark, therefore showing promising in electrochromic devices.[124] The Mg_2(NDISA) and Ni_2(NDISA) MOFs reported by Alkaabi *et al.* exhibited well-behaved quasi-reversible redox events associated with the (NDI)/$(NDI)^-$ and $(NDI)^-$/$(NDI)^{2-}$ redox couples, which were responsible for the electrochromic switching.

4.2. Triphenylamine (TPA)

Triarylamines are tri-substituted aromatic amines in which the central N atom is planar and the pendant aromatic rings are oriented in a "propeller-like" orientation, with each of the phenyl rings canted in the same direction.[125] Triarylamines are capable of easily oxidize by one-electron extraction, which can be achieved through electrochemical or chemical processes to form a stable radical cation.[126] This redox process has been utilised *e.g.* by Cheon *et al.* in the MOF-driven formation of palladium nanoparticles with enhanced H_2 adsorption capacity.[127]

A new multifunctional coordination framework, $[Mn(TPPA)Cl\cdot 3MeOH\cdot DMF]_n$, containing the redox-active TPPA ligand was recently reported by Hua *et al.*[53] The radical cation state of the framework was successfully generated and characterized to be ligand-centred. Importantly, the fluorescence response in this MOF was dependent on the redox state of the framework, demonstrating the potential future application of these materials in host–guest sensing. This material exhibited multifunctionality by virtue of its ability to switch the fluorescence 'on' and 'off' with the redox state promoted by the oxidation of the TPPA ligand. The radical TPPA formation was further characterized by Hua *et al.* in the $[Zn(TPPA)(NO_2)_2\cdot x MeOH\cdot x DMF]_n$ framework by means of *in situ* UV/vis/near-IR, EPR, and fluorescence spectroelectrochemical experiments.[128] The properties of the ligand and the framework were elucidated and quantified as a function of the redox state of the triarylamine core, suggesting that the radical generated was delocalised throughout the ligand backbone. The combination of solution and solid-state *in situ* spectroelectrochemical experiments provides valuable understanding of MOFs as a function of its redox state, which stands promising in the development of materials for energy storage and electrocatalysis.

Recently, a tricarboxytriphenyl amine ligand was combined with a redox-active metal centre to generate a triphenylamine-based MOF material, Cu-TCA.[108] Cu-TCA is a highly porous material (pore radius of *ca.* 1 nm), with Cu^{2+} ions located at the metal paddlewheel cluster sites and N atoms bonded with three neighbour benzene rings to form triphenylamine organic ligands. This novel MOF reported by Peng *et al.* exhibited redox activity both in the metal clusters (Cu^+/Cu^{2+}) and organic ligand radicals ((TCA)/$(TCA)^+$), and was applied as a novel cathode active material for Li batteries. The authors demonstrated that capacity loss took place around the metal clusters (Cu^+/Cu^{2+}), probably due to the restriction of the Li^+ ions by carboxylic oxygen atoms, leading to the incomplete redox reactions on the Cu ions and the structural instability of the whole system. This understanding might help in designing improved MOF-based cathode materials for application in battery sciences.

4.3. Tetrathiafulvalene (TTF)

TTF and its derivatives are well-known electron donors that can reversibly oxidize into their corresponding radical cation $(TTF)^{\bullet+}$ and dication $(TTF)^{2+}$ species. Since the discovery of the semiconducting donor–acceptor TTF–TCNQ salt back in 1973,[129] TTFs have been widely employed to build assorted functional materials for use in molecular conductors, molecular switches, or solar-energy transformators.[130] TTF units have extensively been incorporated in functional coordination polymers; for a comprehensive review, see ref. 131. However, MOFs containing the TTF fragment in the organic linker have just flourished since the seminal work of Narayan *et al.* in 2012.[43]

Inspired by the fact that most electroactive frameworks present high carrier mobility due to the formation of π-stacked arrangements of organic molecules, the TTF unit in the H_4TTFTB ligand was intelligently used as a scaffold to build up a MOF with columnar TTF stacks, constituting the first example of a permanently porous MOF with high charge mobility (Fig. 7a).[43] In this MOF, SBUs are helical chains of corner-sharing metal–oxygen polyhedra joined by helical stacks of benzoates pertaining to $TTFTB^{4-}$. Importantly, EPR experiments demonstrated that the TTF cores were partially oxidized during the MOF synthesis, so this partial doping might be key for its unprecedented intrinsic charge mobility. Subsequently, isostructural metal–organic frameworks M_2(TTFTB) with M = Mn, Co, Zn, and Cd, were reported by Park *et al.*[33] In the series, the Zn, Co, and Mn materials exhibit corner-sharing pseudo-

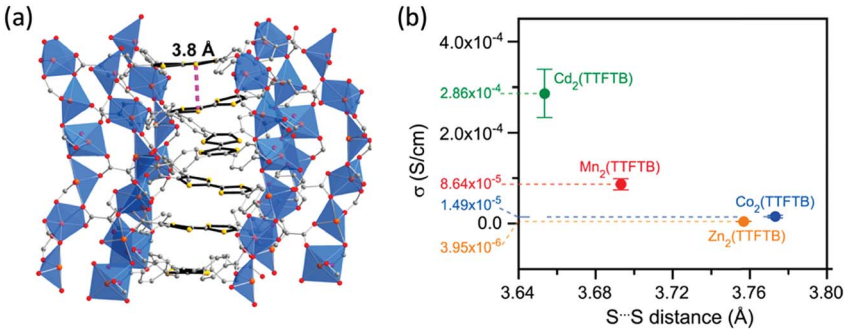

Fig. 7 (a) Side view of a helical TTF stack with a depiction of the shortest intermolecular S···S contact in the crystal structure of Zn_2(TTFTB). (b) Correlation between S···S distance and electrical conductivity in the M_2(TTFTB) MOF family. Reprinted with permission from ref. 33 and 43 Copyright © 2012 and 2015 American Chemical Society.

octahedra, whereas Cd_2(TTFTB) exhibits alternating seven- and six-coordinate metal ions. The authors reported a striking correlation between their single-crystal conductivities and the shortest S···S interaction defined by neighbouring TTF cores (Fig. 7b). Counterintuitively, the shortest S···S distances were found for the larger ionic radius of the metal ions, caused by a pinching that increases the p_z orbital overlap between neighbouring S and C atoms.

Chen *et al.* reported the formation of a MOF constructed from tetranuclear cluster nodes built through the μ^2-O bridge of the TTF ligand, which is first found for TTF coordination polymers.[132] The authors demonstrated that the channel generated by the 3D MOF exerts a confinement effect on the formation of TTF dimers. The TTF dimers showed strong intradimer interaction with partial charge transfer. As a result, the Cd-based MOF provided an enhanced photocurrent response compared to other 2D Cd-MOFs of the same family.

Later, Wang *et al.* rationally constructed two novel frameworks by combining the redox-active ligand TTFTP with spin-crossover Fe(II) centres.[133] The materials exhibited redox activity in addition to thermally and photo-induced spin crossover (SCO). A crystal-to-crystal transformation induced by I_2 intercalation was demonstrated. Although the conduction mechanism could not be elucidated, the oxidative doping markedly enhanced long-range charge transport (up to 3 orders of magnitude) by increasing the density of free charge carriers through $(TTF)^{\cdot+}$ and $(TTF)^{2+}$ formation. Additionally, the SCO behaviour could be modified, and the photo-magnetic behaviour switched off. This work exemplifies a new strategy to tune the spin state and conductivity of framework materials through guest-induced redox-state switching of the ligand.

Only recently, the flexibility of the TTF moiety has been exploited to generate MOFs with unprecedented breathing behaviour. In particular, Su *et al.* coupled redox-switchable properties with breathing behaviour induced by guest molecules in a single framework.[134] The reported In(Me_2NH_2)(TTFTB) MOF experienced a bending of the metal–ligand bonds and a sliding of interpenetrated frameworks upon N_2 adsorption. Reversible oxidation and reduction of TTF moieties in the material changed the linker flexibility, which in turn switched the breathing behaviour. Alternatively, the breathing motion in flexible MOFs can originate differences in electrochemical response, as exemplified in the TTF-based MUV-2 containing the [$Fe_3(\mu_3$-O)$(COO)_6$] SBU.[109] We have reported the breathing behaviour of MUV-2 as a function of solvent conditions promoted by the flexibility of the boat-shaped TTF ligand, and translated into a significant tunability of the pore size along with a dramatic change in the electrochemical oxidation response.[110] The redox-switchable breathing motion of hybrid materials might become an interesting proposition to design bespoke stimuli-responsive MOFs for electrochemical sensing.

4.4. Quinoid–aromatic transition

Quinones are a class of organic compounds that can formally be derived from aromatic derivatives by conversion of an even number of –CH= groups into –C(=O)– groups with any necessary rearrangement of double bonds, which results in a fully conjugated cyclic dione structure.[135] Quinones are usually electron deficient, and their quinoid-like configuration can easily evolve by electron-insertion (reduction) to the corresponding aromatic-like structure (Fig. 6). Likewise, the aromatic structure of a (pro-quinoid) system can easily be oxidized/reduced to generate the corresponding quinoid form, such as in the widely-used thiophene conjugates.[136]

A recent example elegantly exploiting the non-innocence nature of redox-active ligands showing a quinoid–aromatic transition was reported by Cozzolino *et al.* in 2014.[111] The authors demonstrated that Mn_2(DOBDC) can be stoichiometrically oxidized by one electron per metal centre. Surprisingly, the Mn ions maintained a formal oxidation state of +2, suggesting instead the oxidation of the $(DOBDC)^{4-}$ ligand to the quinone $(DOBDC)^{2-}$. The proposed mechanism involved the

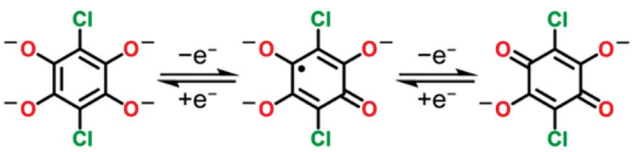

Fig. 8 Redox series of deprotonated benzoquinoid linkers based on chloranilic acid. Left to right: $(DCDHBQ)^{4-}$, $(DCDHBQ)^{3-\cdot}$ and $(DCDHBQ)^{2-}$.

transient formation of a Mn(III) species that eventually evolve back to its initial oxidation state Mn(II) through sequential one-electron transfer processes.

Gui *et al.* reported a redox-switchable MOF that can undergo a reversible single-crystal-to-single-crystal (SCSC) transformation through a hydroquinone/quinone redox reaction.[137] The material exhibited interesting changes in spectroscopic properties through the reversible SCSC transformation and, thus, may be a starting point for the use of such materials in memory storage or redox-based electronic devices. Otherwise, the magnetism and conductivity for a redox pair of Fe–quinoid MOFs has been recently reported by DeGayner *et al.*[138] The oxidized compound, $(Me_2NH_2)_2[Fe_2(DCDHBQ)_3]\cdot 2H_2O\cdot 6DMF$ underwent a SCSC one-electron reduction to give $(Cp_2Co)_{1.43}(Me_2NH_2)_{1.57}[Fe_2(DCDHBQ)_3]\cdot 4.9DMF$. Importantly, this reduction was ligand-based (Fig. 8), being the trianionic framework formulated as $[Fe_2^{III}((DCDHBQ)^{3-\bullet})_3]^{3-}$. Magnetic measurements for this reduced compound revealed the presence of dominant intralayer metal–organic radical coupling to give a magnetically ordered phase below $T_C = 105$ K, one of the highest reported ordering temperatures for a MOF, as well as high electrical conductivity.

TCNQ is a well-known acceptor quinoid molecule, which can be easily reduced to form the open shell radical anion $(TCNQ)^{\bullet -}$ with aromatic structure. Although the incorporation of TCNQ in a MOF is most notably exemplified in the host–guest HKUST@TCNQ MOF,[39] which led to unprecedented electrical conductivity, TCNQ can also build up frameworks as a ligand itself.[112,139] Zhang *et al.* reported the formation of a family of semiconducting main-group metal–organic frameworks, namely, $[Tl(TCNQX_2)]$, (X = H, Cl, Br, I), for which charge mobility was suggested to occur not only in 1D but rather be multidimensional, implying $(TCNQ)^{\bullet -}$ radical formation.[112]

Pyrene is a polycyclic aromatic hydrocarbon that has been widely used due to its intrinsic electronic properties, conferring emission of light in the blue region of the solar spectrum. It can be easily oxidized to promote a quinoid-like structure, as evidenced recently in pyrenedione derivatives.[140] Pyrene has also been incorporated in MOFs, most extensively exploited for the generation of fluorescent materials.[141] However, some examples of redox-active MOFs based on the pyrene moiety have also been reported. Kung *et al.* demonstrated in 2013 the generation of a MOF thin film that exhibited electrochromic switching between yellow and deep blue by means of a one-electron redox reaction at its pyrene-based linkers.[120] Only recently, Bandyopadhyay *et al.* have reported a novel class of conjugated porous organic polymers having an N-containing network, where the decoration of pyrene ligands with electron-rich aryl-diamine groups led the material to be an excellent electrode for supercapacitor energy storage applications.[142]

The redox properties of catechol can also be strategically utilised towards the formation of intermediate *ortho*-benzoquinone, which finally leads to cyclopentadienone. In a recent work of Huang *et al.*, a catechol functionalized ligand was used as the redox-active pillar to construct a pillared-layer framework.[143] The metal carboxylate framework $(H_3O)_2[Co_6O(DHBDC)_2(H_2DHBDC)_2(EtOH)_4]\cdot 2EtOH$ (denoted as MCF-13 or 3D-Co) crystallizes in the $I\bar{4}2m$ space group with a unique 3D pillared-layer structure consisting of wave-like $\{Co_6O(DHBDC)_2\}^{2+}$ layers and H_2DHBDC^{2-} pillars. When the 3D pillared-layer MOF serves as an electrocatalyst for water oxidation, the pillar ligands can be oxidized *in situ* and removed (Fig. 9). The resulting 2D ultrathin nanosheets possessed an exceptionally high oxygen evolution reaction activity with low overpotentials (211 mV at 10 mA cm^{-2}) and a high turnover frequency (30 s^{-1} at an overpotential of 300 mV).

4.5. Redox-active metal-containing linkers

Porphyrins. Metal-containing linkers (or metalloligands) are becoming a popular means of easily incorporating redox activity.[144] Metalloporphyrins have shown promise in promoting the reduction of various substrates, and their unique spectral properties make them ideal candidates for spectroelectrochemical studies.[145,146] Various porous materials comprised of porphyrins have been developed,[147] including porphyrinic MOFs with open accessibility to redox-active metal centers.[148–150] Only recently, the first phthalocyanine-based MOF has been reported by Nagatomi *et al.*[151] This 2D MOF was used

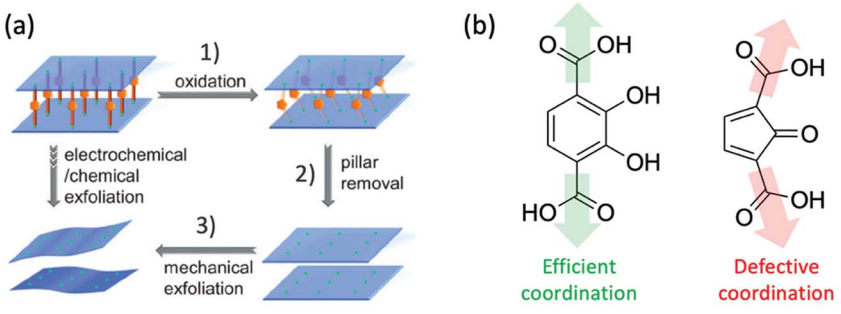

Fig. 9 (a) Electrochemical/chemical exfoliation of a pillared-layer MOF: (1) selective oxidation of catechol-based H_4DHBDC ligand to form 2-oxocyclopenta-3,5-diene-1,3-dicarboxylic acid; (2) spontaneous removal of the ligand pillars due to inefficient bridging angle (weak coordination ability); and (3) exfoliation of the intermediate crystalline phase to ultrathin nanosheets. (b) Chemical structure of the initial catechol pillar (left), and the oxidized 2-oxocyclopenta-3,5-diene-1,3-dicarboxylic acid (right). Reprinted with permission from ref. 143. Copyright © 2018 John Wiley & Sons, Inc.

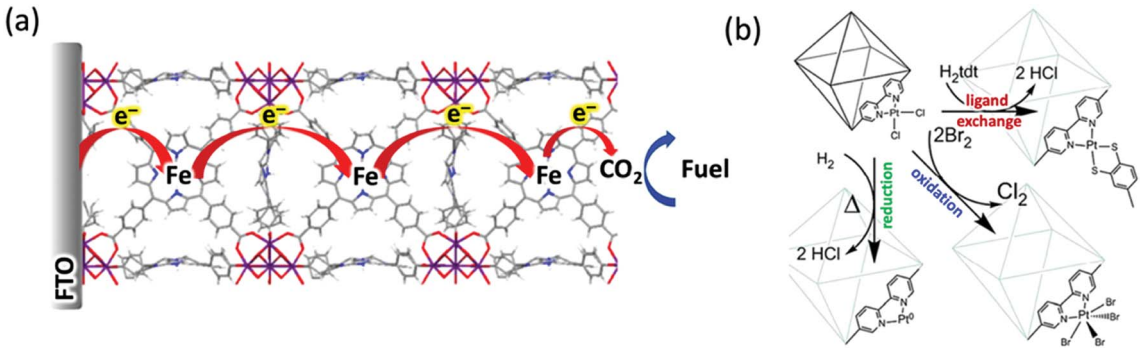

Fig. 10 (a) Representation of the charge hopping transport mechanism in Fe-MOF-525 towards the electrochemical reduction of CO_2. (b) Schematic picture of the reactivity of Pt(II) species in functionalized Pt-UiO-67 MOFs. Reprinted with permission from ref. 113 and 114. Copyright © 2015 American Chemical Society.

as a high-performing cathode in Li batteries owing to the electrically conductive and redox-active hierarchical microporous/mesoporous structure.

Ahrenholtz *et al.* reported in 2014 a thin film of a metalloporphyrin metal–organic framework (CoPIZA) consisting of CoTCPP struts bound by linear trinuclear Co(II)-carboxylate clusters.[48] The film was shown to be electrochemically active, retaining its structural integrity with applied potential, with reduction processes associated to Co(II/III) and Co(I/II) redox pairs and supporting a redox hopping mechanism of charge transport. Importantly, the CoPIZA thin film demonstrated catalytic activity for the reduction of carbon tetrachloride upon reduction of the metalloporphyrin struts to (Co(I)TCPP)CoPIZA.

Kung *et al.* reported the growth of thin films of a MOF constructed from free-base porphyrin linkers and hexa-zirconium nodes (MOF-525) that exhibited electrocatalytic activity for the oxidation of nitrite.[152] Subsequent studies on the post-metalated Zn-MOF-525 and Co-MOF-525 led to thin films electrochemically addressable in aqueous solution for further electrocatalytic applications.[153] Using the Fe-MOF-525 analogue, Hod *et al.* found that the well-known CO_2 reduction catalyst Fe-TPP can be installed on electrode surfaces at almost an order of magnitude higher than the highest previous report on heterogenized molecular CO_2 reduction catalysts.[113] Importantly, the MOF's metalloporphyrinic linkers serve as both electrocatalysts and as redox-hopping-based conduits for the delivery of reducing equivalents to catalytic sites that are not in direct contact with the underlying electrode (Fig. 10a).

Porphyrin-based linkers have also been utilised to gain insight into the mechanism of the catalytic reduction of O_2 (ORR). Lions *et al.* reported electrochemical studies on Co-Al-PMOF, suggesting that the ORR reaction occurs in the CoTCPP cobalt porphyrin environment.[154] The presence of four labile protons in the CoTCPP molecule might act as a promoter for the proton transfer step by locally activating the O–O bond cleavage and thus contributing to a more efficient reduction reaction towards water. Gallagher *et al.* have managed to isolate the first rigorously four-coordinate Mn(II) porphyrin complex by means of a MOF scaffold. The authors demonstrated the complexation of O_2 through a peroxo ligand formation bound in a side-on, η^2 mode to an $S = 3/2$ Mn(IV) ion. The binding of O_2 in PCN-224 was found to be reversible and its strength was shown to increase with increasing reductive capacity of the Mn(II/III) redox, allowing rational design of MOF materials with improved ORR efficiencies.

Bipyridine and catechol metalloligands. Incorporation of metal complexes in chemically active organic ligands other than N-based macrocycles has also been applied to promote redox-activity.[144] For instance, biphenyl and bipyridine can exchange in the UiO-67 crystal in any ratio due to their structural similarity, thus opening the possibility to utilize the chelating ability of bipyridine as a backbone ligand for catalytically active metal complexes (Fig. 10b). This principle has been recently materialized by Oien *et al.* in zirconium-based UiO-67 functionalized with Pt bipyridine coordination complexes ((BPyDC)Pt(II)Cl_2 and (BPyDC)Pt(IV)Cl_4) acting as linkers to be exploited in redox catalysis.[114] Further studies of Braglia *et al.* allowed modification of the coordination vacancies to the formation of very small Pt nanoparticles hosted inside the MOF cavities,[155] or the insertion of Cu(II) to alter the redox properties of the material.[156] Similarly, UiO-67 was "expanded" and "contracted" by Wang *et al.* using bipyridine and phenylpyridine linkers, respectively, towards the inclusion catalytically active IrCp*Cl sites.[157,158] These MOFs were active in chemically promoted water oxidation using ceric ammonium nitrate.

Making profit of a MOF scaffold provides the opportunity to reveal mechanistic details in well-defined single-site solid catalytic systems that are difficult to obtain from their homogeneous counterparts. Lin *et al.* have recently reported the synthesis of $[Ru(TP)(BPyDC)(OH_2)]^{2+}$ doped UiO-67 MOF to deepen in the understanding of chemical water oxidation.[159] Their results indicated that the MOF catalyst exhibits a single-site reaction pathway with kinetic behaviour similar to that of a homogeneous Ru complex, and suggested that the rate of redox-hopping charge transport is sufficient to promote chemistry throughout the MOF particulates. Otherwise, Li *et al.* reported a series of mixed-linker bipyridyl MOF-supported palladium(II) catalysts for Suzuki–Miyaura cross-coupling reactions.[160] The authors demonstrated that the stereoelectronic properties of metal-binding linker units are critical to the activity of single-site organometallic catalysts in the MOF.

Finally, two new UiO-68 type of Zr-MOFs featuring redox non-innocent catechol-based linkers of different redox activities have been recently synthesized by Zhang *et al.*[161] Metalation of the MOFs with Cu(II) precursors triggered the reduction of copper by the phenyl-catechol groups to Cu(I) with the concomitant formation of semiquinone radicals. The MOF-supported catalysts were selective toward the allylic oxidation of cyclohexene, and it was found that the presence of *in situ*-generated Cu(I) species is correlated with an enhanced catalytic activity.

5. Host–guest redox activation

The incorporation of a redox-active guest into a framework is one of the most exploited strategies to engender redox activity in MOFs (see Table 3 for a list of recent examples). Up to date, two methods are mostly used for this purpose: the covalent grafting of electroactive organic or inorganic moieties, usually in the metal node, or the insertion/encapsulation of a wide variety of species (ranging from small organic molecules to large metallic nanoparticles) in the pores of the framework by means of noncovalent interactions.

5.1. Ferrocene

In the seminal work of Meilikhov *et al.*,[171] the first example of a third concept of post-synthetic MOF functionalization was reported, which targeted surface exposed OH-groups that bridge the metal centres of the secondary building units through reaction with a ferrocene derivative (FDMS). Despite the loading of the channels with ferrocenyl substituents, the material could adsorb reversibly small molecules such as benzene, and catalysed the liquid-phase benzene oxidation to selectively obtain phenol. Reduction of the ferrocenyl loading is subsequently straightforward, thus giving way to increase the catalyst efficiency by increasing the mobility of species inside the channels.

Following studies of Meilikhov *et al.* reported a selection of metallocene inclusion compounds with channel structured MOFs by means of noncovalent interactions.[162] The inclusion of redox-active guests resulted in the induction and enlargement of the breathing effect of the inorganic backbone in Al-MIL-53. More interestingly, the inclusion of redox-active cobaltocene into V-MIL-47 led to the formation of a charge-transfer compound with a negatively charged framework that crystalizes in an *Imma* space group. The reduction of the vanadium centres was found to be stoichiometric, and the resulting material turned out to be a mixed-valence compound with a V(III/IV) ratio of 1 : 1.

Later, Halls *et al.* demonstrated the incorporation of redox-active ferrocene moieties towards covalent linkage to a BDC organic linker in Zn(II) and Al(III) dicarboxylate frameworks.[172] In organic media, well-defined and stable redox processes associated with the oxidation and back-reduction of the pore surface ferrocenes were observed, related to a rapid hopping of charges across the MOF surface. However, voltammetric responses for the ferrocene oxidation exhibited rapid decay in aqueous media due to dissolution of the functionalised MOF framework. Likewise, Hod *et al.* reported the installation of ferrocene molecules within the wide-channel NU-1000 MOF.[47] The 3D structure of NU-1000 can be described as 2D Kagome sheets linked by TBAPy ligands, where the parent-framework node consists of an octahedral Zr_6 cluster capped by eight μ_3-OH ligands. Due to the large porosity of NU-1000 (pore diameter of 30 Å in the hexagonal mesopores and of 12 Å in the triangular micropores), the authors could controllably install one ferrocene molecule per inorganic node. The MOF rendered electroactive in the vicinity of the ferrocenium/ferrocene (Fc^+/Fc) redox potential. Patwardhan *et al.* theoretically characterized the charge-transfer phenomena in this ferrocene-based NU-1000 material, demonstrating that charge can be transferred across the ferrocene units either *via* direct hopping or through a linker-mediated superexchange mechanism.[173]

Coupling electron exchange to the oxidation-state-dependent formation of inclusion complexes is a viable proposition to switch redox activity. Hod *et al.* found that host–guest noncovalent interactions can be exploited to modulate rates of hopping-based charge transport through MOF thin films.[38] This modulation was attributed to the preferential host–guest complex formation with ferrocene relative to ferrocenium when adding cyclodextrin guest. The kinetics of site-to-site of charge hopping and, in turn, the overall redox conductivity, of the ferrocene-modified MOF could be increased by up to 30-fold.

Very recently, Van Wyk *et al.* have characterized the charge-transfer (CT) complex between the photoexcited TBAP linker and a node-anchored ferrocene moiety in a Zr-based MOF.[37] The CT reaction occurring within the mesoporous framework NU-

Table 3 Summary of novel host–guest redox-activated MOFs

MOF	Guest	Host–guest interaction	Applications	Ref.
V-MIL-47	Cobaltocene	Covalent	Mixed valency; charge-transfer compounds	162
NU-1000	Ferrocene	Covalent	Sensing; photo/electrocatalysis	47
UMCM-1	Methylene blue	Noncovalent	Electrocatalysis	163
UMCM-1	Alizarin red S	Noncovalent	Energy storage	164
$\{(H_2BP)[Cd_3(BTC)_2]\cdot 2H_2O\}_n$	Viologen	Noncovalent	Data storage; bioimaging	165
$(TTF)[\{Ru_2^{II,II}(2,3,5,6\text{-}F_4PhCO_2)_4\}_2(TCNQ)]$	Tetrathiafulvalene	Noncovalent	Lithium-ion batteries	166
NU-1000	[2]catenane	Mechanically interlocked	Molecular electronic devices	167
ZIF-8	Fe_3O_4 nanoparticles	Noncovalent	Non-enzymatic glucose sensor	168
UiO-66-NH_2	Pt nanoparticles	Noncovalent	Photocatalysis	169
MIL-101	PdAg nanoparticles	Noncovalent	Heterogeneous tandem catalysis	170

1000 to lead $[NU\text{-}1000]^{\bullet -}/(Fc)^{+}$ implied the formation of the negative radical $(TBAP)^{\bullet -}$ species. Dielectric-dependent CT kinetics indicated that the process involved a high reorganisation energy, required to polarize the node bound-hydroxyl/aqua ligands. A strategy to eliminating the node-bound polar hydroxyl/aqua ligands might therefore become relevant for future design of improved MOF-based electrocatalytic and photoelectrochemical systems.

5.2. Molecular organic guests

Guest inclusion of organic molecules employing noncovalent interactions for encapsulation is increasing in popularity as an alternative strategy to promote redox activity in metal–organic frameworks. Note that we do not consider composite materials in which the MOF is not the main scaffold or hybrid systems formed by surface coating of interface contacts.[174–176]

Small redox-active organic molecules can be readily adsorbed into redox-inactive MOFs to promote electroactivation, as demonstrated in the seminal work of Halls *et al.* in 2012.[163] They reported the incorporation of methylene blue as an absorbed redox-active dye component into the redox-inactive UMCM-1. An irreversible adsorption process with high pore loading led to a change in coloration during dye adsorption, while the reactivity of the pore-bound methylene blue remained

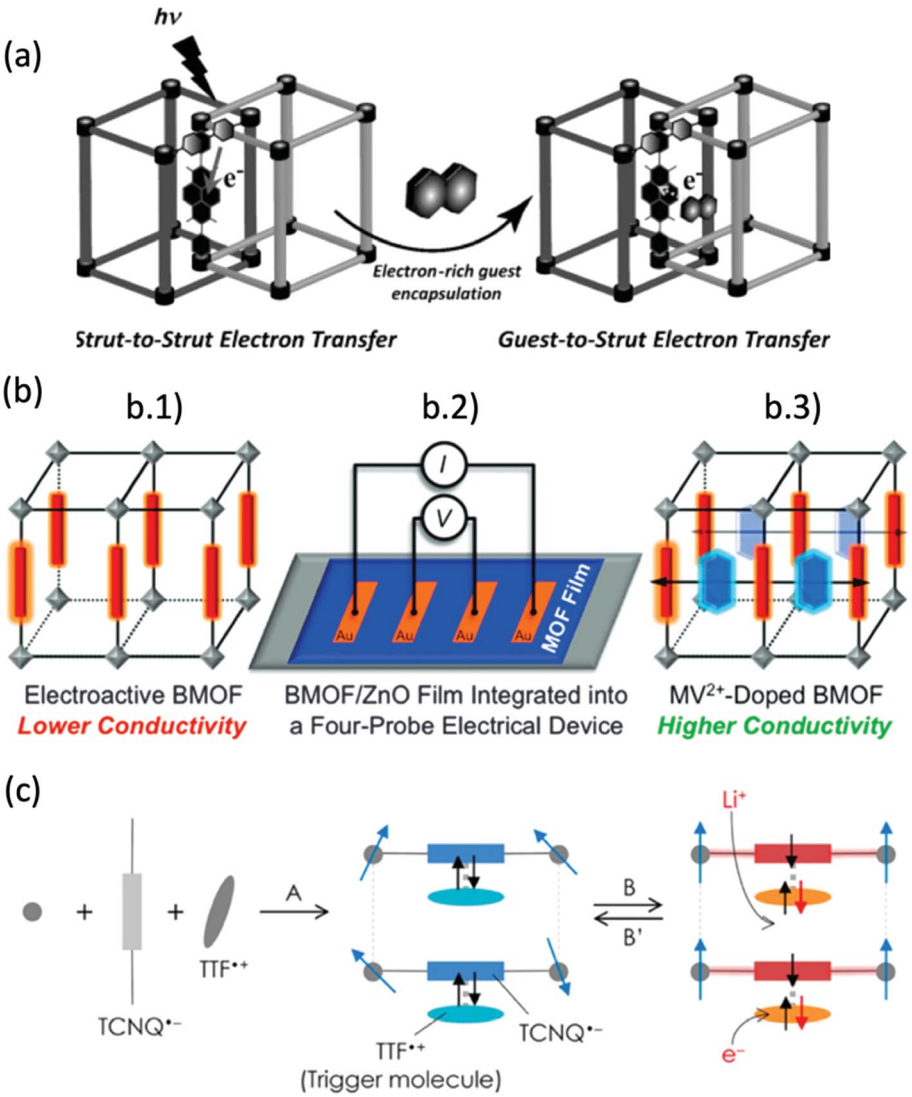

Fig. 11 (a) Schematic diagram of the strut-to-strut/guest-to-strut electron transfer in multichromophoric redox-active interpenetrated 3D $\{[Cd(BPDC)(BPNDI)]\cdot 4.5H_2O\cdot DMF\}_n$ framework. (b) Graphical illustrations of (1) an electroactive MOF made of redox-active ligands, (2) a four-probe electrical device composed of the electroactive MOF film grown selectively on a ZnO-coated surface, and (3) intercalation of π-acidic guests between the redox-active ligands leading to a better electron delocalisation through the resulting π-D/A stacks and higher conductivity. (c) Schematic representation of the design strategy for functional MOFs where the pre-organization of functional parts with trigger molecules (step A) and post-treatment for functionalization tuning (step B) are assembled in a single system. Reprinted with permission from ref. 36,166 and 178. Copyright © 2016 Royal Society of Chemistry, and Copyright © 2015 and 2018 John Wiley & Sons, Inc.

unchanged. One year later, the inclusion of the redox-active dye alizarin red S into UMCM-1 was demonstrated.[164] Intriguingly, the authors showed that alizarin red S redox processes in UMCM-1 immersed in several media were surface-confined, and dominated by the potential driven reductive release of leuco-alizarin red S into the surrounding solution. Expulsion of the ionized guest species upon electrochemical treatments is one of the main drawbacks when incorporating redox-active guests in MOF scaffolds by means of weak noncovalent interactions.

Host–guest interactions can modulate magnetic and photochromic properties of the MOF scaffold. For example, Zhang *et al.* reported the tunability of spontaneous magnetization behaviours at low temperatures within a MOF through inclusion of several aromatic molecules (benzene, toluene, aniline and nitrobenzene) in the redox-active Fe(TCNQ)(BP).[177] Otherwise, Sikdar *et al.* reported a redox-active porous interpenetrated framework, $\{[Cd(BPDC)(BPNDI)]\cdot 4.5H_2O\cdot DMF\}_n$, where the m-oxo-bridged secondary building unit guided the parallel alignment of BPNDI acceptor linkers, to form a photochromic material.[36] Encapsulation of electron-donating aromatic molecules in the electron-deficient channels of the MOF led to a perfect donor–acceptor co-facial organization, resulting in long-lived charge-separated states promoted by a guest-to-strut electron transfer (Fig. 11a). Similarly, Xing *et al.* reported a new electron-transfer photochromic MOF compound ($\{(H_2BP)[Cd_3(BTC)_2]\cdot 2H_2O\}_n$; space group: *Ibam*) through encapsulation of photoactive viologen $(H_2BP)^{2+}$ cations.[165] This material was demonstrated to exhibit a charge-separated state with a lifetime value of more than 2 months, exceeding reported values for analogue frameworks, thanks to the formation of π⋯π stacking interactions around the reduced $(H_2BP)^{+\bullet}$ radicals. Metal–organic frameworks with stable charge-separated states underpins the development of new materials with photoswitchable luminescence for data storage, bioimaging, barcode and other novel applications.

The conductivity of MOFs can be fine-tuned by complementary guest π-systems through promotion of long-range electron delocalization.[178] Guo *et al.* constructed a blue-coloured pillared-paddlewheel MOF, namely BMOF, composed of redox-active BPDPNDI pillars and TCPB struts, and grew stable, uniform BMOF films on ZnO substrates *via* a bottom-up approach (Fig. 11b). Stronger π-acidic guests ($(MV)^{2+}$ > DFDNB > DNT) enhanced the conductivity of BMOF more significantly than the weaker ones, suggesting that strong donor/acceptor interactions between the guest and the BPDPNDI ligands trigger effective charge delocalisation through the formation of π-stack assemblies.

The electron-rich TTF unit has also been subject of intensive research to be implemented as a guest in order to promote redox activity in MOFs. Fukunaga *et al.*[166] reported a $(TTF)^{\bullet+}$–$(TCNQ)^{\bullet-}$ salt incorporated into a paddlewheel-type Ru-based MOF, $(TTF)[\{Ru_2^{II,II}(2,3,5,6\text{-}F_4PhCO_2)_4\}_2(TCNQ)]$, which crystallizes in a *C*2/*c* space group. $[Ru_2]$ and $(TCNQ)^{\bullet-}$ units result in a coordination framework with the formula $[\{Ru_2\}_2(TCNQ)]^{-}{}_\infty$, and the $(TTF)^{\bullet+}$ cations are coulombically held in the pores of the framework forming an irregular π-stacking alternating column with the $(TCNQ)^{\bullet-}$ strut. In this case, $(TTF)^{\bullet+}$ acts as a "trigger molecule (ion)" for controlling the magnetic phase of the material, which can induce the intrinsic magnetic nature of the framework through electrochemical reduction activation of the $(TTF)^{\bullet+}$–$(TCNQ)^{\bullet-}$ set (Fig. 11c). This material was further incorporated as a cathode in a Li-ion battery, and the reversible magnetic phase switching between the non-volatile ferrimagnetic and paramagnetic states was demonstrated through the discharge/charge cycling process.

Guo *et al.* have recently constructed a new honeycomb-shaped electroactive MOF-74 from an electron-deficient NDI ligand equipped with two terminal salicylic acid groups.[32] π-Intercalation of the electron-rich TTF guest between the NDI ligands stacked along the walls allowed lowering the electronic bandgap of the material by *ca.* 1 eV. Improved electron delocalisation through the guest-mediated π-donor/acceptor stacks was attributed to the smaller bandgap in the doped material, which forecasts an improved electrical conductivity. This concept can be extended to virtually any MOF architectures that furnish parallel electroactive ligands at regular intervals and are capable of forming guest-mediated π-donor/acceptor stacks.

Finally, rotaxanes have also been incorporated in appropriately functionalized MOFs to build multidimensional mechanically interlocked machineries (MIMs) by making use of guest grafting and mechanical bonding. McGonigal *et al.* successfully incorporated a semirotaxane consisting of a viologen-containing thread and a tetracationic macrocycle into the robust zirconium-based NU-1000.[179] Later on, Chen *et al.* reported the immobilization of bistable [2]catenane-based molecular switches into NU-1000.[167] Cyclic voltammetry characterizations proved the reversibly redox-switchable molecular circumrotations of MIMs in the solid state (Fig. 12). Additionally, the bistable [2]catenanes in NU-1000 could be chemically oxidized/reduced in a reversible manner. This technological advance represents an important step toward incorporating bistable mechanically interlocked molecules into robust, highly porous 3D frameworks as prototypes for molecular electronic devices.

5.3. Metal nanoparticle-based composites

The permanent porosity of many MOFs enables their ability to confine small metal nanoparticles (NPs).[180] The use of MOFs as

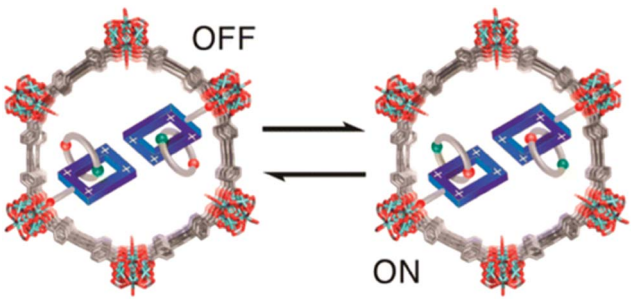

Fig. 12 Schematic of the switch 'on/off' mechanism of functionalized bistable [2]catenane incorporated into NU-1000. Reprinted with permission from ref. 167. Copyright © 2016 American Chemical Society.

the shell provides important benefits as: (i) a protective layer to prevent NPs from aggregating and migrating during the calcination process; (ii) narrow penetrating channels to support the transport of micromolecules; (iii) large surface areas and inherent porosity to facilitate the migration of reactants on the NPs surface; and (iv) maintenance of the catalytic activity over multiple catalytic cycles.[180] The electrocatalytic properties of noble NPs combined with the large surface area of the MOFs provide new electrode materials for various electrochemical and biochemical sensors.[175] In this regard, improved electrochemical sensors with enhanced electrocatalytic performances have been constructed based on Ag NPs/MIL-101 composites for tryptophan analyte,[181,182] bimetallic AuPd NP decorated UiO-66-NH_2 composites for nitrite,[183] or Pd@Co/MIL-101 heterostructures for the hydrolytic dehydrogenation of NH_3BH_3.[184]

Recently, MOFs have also been used as host materials for fabricating core–shell heterostructures through encapsulation of metal oxide NPs.[176,180] The combination of magnetic Fe_3O_4 NPs, reduced graphene oxide (RGO), and MOFs (*i.e.* Fe_3O_4@ZIF-8/RGO) was reported for electrochemical sensing of dopamine in the presence of ascorbic acid and uric acid.[168] Similarly, copper oxide nanoparticles have been incorporated into MOFs to build up enhanced non-enzymatic glucose sensors, such as that reported by Shi *et al.* using Cu/Cu_xO_x NPs in a ZIF-8 composite,[185] or for the electrocatalytic determination of H_2O_2, as in the core–shell heterostructure of Cu_xO NPs@ZIF-8 reported by Yang *et al.*[186]

On the other hand, MOFs can selectively allow substrates/products that are smaller than the MOF pores to pass through and access the NPs (active sites), while blocking larger molecules. Stephenson *et al.* substituted the 2-methylimidazolate linkers in Pt@ZIF-8 with imidazole to form Pt@SALEM-2. Both catalysts were active for the hydrogenation of 1-octene, whereas the hydrogenation of *cis*-cyclohexene occurred only when using Pt@SALEM-2 as a catalyst, due to its larger apertures. The largest substrate, β-pinene, was unreactive with H_2 when either catalyst was employed, highlighting the size exclusion effect.[187] Similarly, Aguado *et al.* recently employed the imidazolate-based SIM-1 ($Zn(C_{10}H_{10}N_4O_2)$) to construct a core–shell composite with Pt/Al_2O_3 as the core.[188] Due to the narrow pore opening of SIM-1, ethylene could easily cross the SIM-1 shell and be converted to ethane, whereas toluene, with a larger molecular size, was excluded.

The electronic properties of metal NPs can significantly be altered by the MOF platform. Most recently, the group of Jiang observed an interesting electron transfer between metal NPs and porphyrinic MOFs, PCN-224(M), which regulates the electronic state of the Pt surface and thus the catalytic efficiency of alcohol oxidation by changing the intensity of light irradiation.[189] Otherwise, NPs can also act as electron acceptors and active centers, while MOFs behave as photosensitizers and stabilizers. Xiao *et al.* investigated the efficiency of electron–hole separation and charge-carrier process for photocatalysis in a NPs/MOF composite.[169] The authors deliberately synthesized two types of composite: Pt NPs of *ca.* 3 nm were incorporated inside or supported on a representative MOF to afford Pt@UiO-66-NH_2 and Pt/UiO-66-NH_2, respectively, for photocatalytic hydrogen production *via* water splitting. Pt@UiO-66-NH_2 gave a stronger Zr(III) signal and higher activity than Pd/UiO-66-NH_2 owing to an accelerated electron transfer.

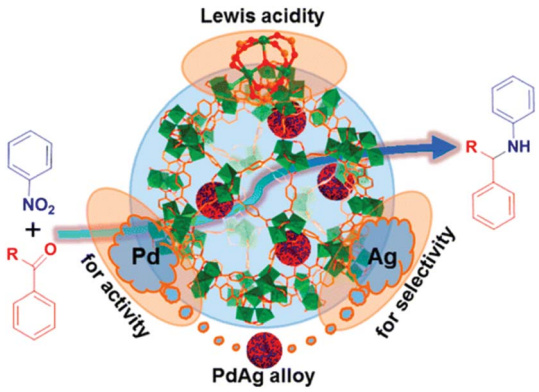

Fig. 13 Scheme of the synergistic characteristics of each component in the catalytic performance of PdAg@MIL-101 composite towards the synthesis of secondary arylamines. Reprinted with permission from ref. 170. Copyright © 2015 American Chemical Society.

Both MOFs and metal NPs can constitute active sites for tandem catalysis. Chen *et al.* synthesized monometallic and bimetallic NPs@MOF catalysts, featuring tiny metal NPs inside MIL-101 cages, for one-pot multistep selective reaction.[170] MIL-101 is comprised of trimeric chromium(III) octahedral clusters interconnected by 1,4-benzenedicarboxylates, resulting in a highly porous 3-dimensional structure. The large pores (29 and 34 Å) and high BET surface area (>3000 $m^2\ g^{-1}$) with a huge cell volume (*ca.* 702 000 $Å^3$), together with the coordinatively unsaturated open metal sites, allow diverse post-synthesis functionalization and guest encapsulation. After nanoparticle encapsulation, the Pd@MOF cooperatively catalyzed a tandem reaction on the basis of both the MOF Lewis acidity and Pd sites. Strikingly, the bimetallic PdAg@MOF composite involving three active sites (Lewis acid, Pd, and Ag) was able to successfully realize a one-pot multistep cascade reaction in the synthesis of secondary arylamines. This process resulted in cooperation between the MOF host and the metal NP guest as well as a synergistic catalytic performance between the bimetallic Pd and Ag species: the MOF affords Lewis acid sites, Pd offers hydrogenation activity, and Ag greatly improves the selectivity toward the desired product (Fig. 13).

6. Charge-transfer frameworks

6.1. Donor–acceptor pairs

The integration of donor and acceptor entities into the framework is one of the most sought procedures to promote charge-transfer (CT) mechanisms and infuse redox activity inside a MOF.[17,190,191] In contrast to the widely investigated organic CT phenomena, understanding of the charge transfer in redox-active MOFs is scarce. Besides their increased dimensionality and structural robustness relative to purely organic systems, the potential void space in MOFs opens the possibility to inspect

unconventional CT phenomena promoted by guest-induced interactions.

Appropriate matching of the electronic energy levels of the different components of a system can be exploited to bring about CT when electron donor (D) and acceptor (A) moieties are arranged in close proximity, interacting either through-bond or through-space. This process can be described by the following reaction:

$$D^0A^0 \leftrightarrow D^{\delta+}A^{\delta-}$$

where the degree of CT (δ) can acquire values between $0 < \delta < 1$.[192] δ is largely dictated by the overlap in frontier electronic orbitals, and by the ionization potential and electron affinity of D and A, respectively. Three possibilities arise depending on the magnitude of δ: a neutral or quasi-neutral state ($\delta < 0.5$), a partial CT or mixed-valence state ($0.5 < \delta < 1$) state, or a fully ionic state ($\delta = 1$). A plot of the energy of the CT band maximum (ΔE_{CT}) *versus* the potential energy difference between D and A results in the so-called Torrance diagram, which describes a boundary between the neutral and ionic states (Fig. 14a).[193,194] The degree of CT controls numerous physical properties of CT salts including the lattice energies, bond lengths, optical bandgaps, and conductivities. Key to CT phenomena in these systems is the presence of components that can possess stable (neutral, anionic or cationic) radical states.

The donor–acceptor assembling strategy has drawn inspiration from the field of organic metals. This area flourished following the discovery of the archetypal CT TTF–TCNQ compound in 1973 by Ferraris *et al.*,[129] which was found to exhibit metallic conductivity (1.47×10^{-4} S cm^{-1} *versus* 6×10^{-5} S cm^{-1} in Cu). However, donor–acceptor MOFs presenting CT phenomena are rare due to the inherent large spatial separation between the different chemical redox-active components in the framework. Miyasaka and coworkers pioneered the research of donor–acceptor D/A-MOFs, and provided a systematic control of the CT phenomena in such materials. Seminal work by Miyasaka *et al.* reported layered materials with chemical formula $[(M_2(O_2CCF_3)_4)_2(TCNQ)]\cdot C_7H_8$, which integrated the electron-rich dinuclear complex $[M_2(O_2CCF_3)_4]$ and the electron-acceptor TCNQ.[195,196] Partial CT was observed from the metal node to TCNQ, which was attributed to a significant metal–ligand π-backbonding. By substituting TCNQ for its more electron-deficient derivative $TCNQF_4$, one-electron transfer from $[Ru_2(O_2CCF_3)_4]$ to $TCNQF_4$ was observed,[197] leading to a strong intralayer magnetic coupling and 100-times greater conductivity. Fig. 14b displays the linear relation between the CT energy (ΔE_{H-L}) and the donor/acceptor ionization potential/electron affinity difference ($\Delta E_{1/2}$) for a wide range of D/A MOF combinations reported up to date. Interestingly, a compound exhibiting a neutral-ionic transition was found at the neutral-ionic boundary (purple triangle in Fig. 14b), thus supporting the use of ionicity diagrams as a design tool for materials discovery.

The combination of a redox-active MOF with porous flexibility and ion-migration capability enables the creation of new pathways toward magneto-electric coupling devices in the field of ionics. In a recent study, Taniguchi *et al.* demonstrated the artificial construction of a ferrimagnetic lattice by doping electrons into acceptor sites of a neutral D/A-MOF.[199] By taking advantage of the rechargeability of battery systems, the reversible control of non-volatile magnetic phases in the D/A-MOF was achieved just one year later.[200]

A metal-bearing coordination network synthesised from $Re(BPyDC)(CO)_3Cl$ bridging ligands and Cu(II) nodes was reported to undergo an irreversible photoinduced charge-transfer process.[201] Upon CT, formal oxidation of Re(I) to Re(II) occurred, accompanied by reduction of Cu(II) centre into diamagnetic Cu(I). This approach opened up the possibility of understanding photo-induced charge-transfer processes within multidimensional frameworks.

Installing charge carriers to increase electron or hole mobility in intrinsically insulating or weakly semiconducting MOFs has proven to be an effective strategy (Table 4). Two recent examples of CT frameworks demonstrate the potential to exploit through-bond and through-space CT mechanisms. In the first case, infiltration of the electron-acceptor TCNQ into HKUST-1 led to a bridging of the dinuclear Cu paddlewheel clusters with the ligands and their partial reduction.[15,39,202,203] The result was a strong through-bond electronic coupling between the units, with a partial charge transfer to TCNQ and

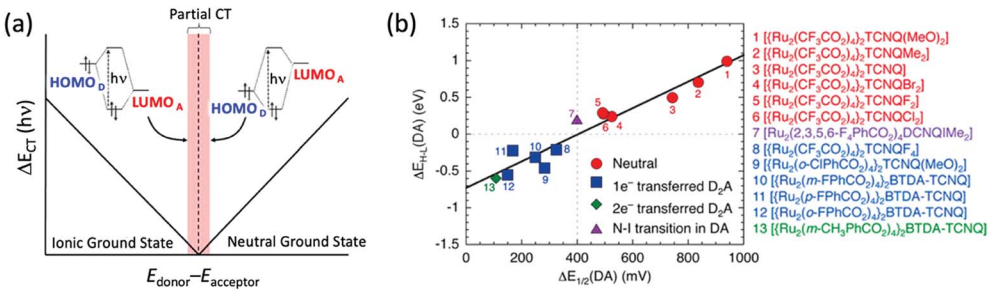

Fig. 14 (a) Schematic of Torrance's "V-shaped" diagram showing the relationship between the energy of CT, ΔE_{CT}, and the difference between donor and acceptor ionization potential and electron affinity ($\Delta E_{1/2}$), respectively. The red region highlights the range in which partial CT and metallic conductivity are observed. (b) Plot of ΔE_{CT} (in this case, the HOMO–LUMO gap or ΔE_{H-L}) *vs.* $\Delta E_{1/2}$ for D_2A and DA materials of $[Ru_2^{II,II}]$/$TCNQR_x$, $DCNQIR_x$. Reprinted with permission from ref. 192 and 198. Copyright © Materials Research Society 2016 and Copyright © 2012 American Chemical Society.

Table 4 Donor–acceptor and mixed-valence MOFs with high charge transport

MOF	Mixed valency	Conductivity (S cm^{-1})	Ref.
HKUST-1@TCNQ	—	0.07	15, 39, 202 and 203
$[K_5Zn_2(BCEBP)_3(OH)_2(H_2O)_2]_n[Pb_6I_{19}]_n$	—	5.52×10^{-6}	204
Cu[Cu(PDT)$_2$]	Cu(I)[Cu(III)(PDT)$_2$]/Cu(II)[Cu(II)(PDT)$_2$]	6×10^{-4}	205
Cu[Ni(PDT)$_2$] (I_2-doped)	[Ni(PDT)$_2$]$^{1-/2-}$	1×10^{-4}	206
[(TBA)$_2$Fe$_2^{III}$(DHBQ)$_3$]	(DHBQ)$^{2-/3-}$	0.16	49
Fe$_2$(DSBDC)	Fe(II/III)	3.9×10^{-6}	207
$K_xFe_2(BDP)_3$	Fe(II/III)	0.025	208
Fe(TRI)$_2$(BF_4)$_x$	Fe(II/III)	0.31	10
Fe$_2$(BDT)$_3$	Fe(II/III)	1.8	11

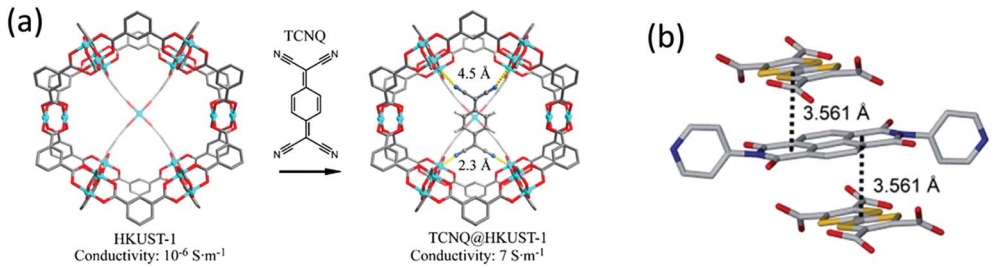

Fig. 15 (a) TCNQ guest incorporation into HKUST to promote a six-fold increase in conductivity. (b) Noncovalent stacking of the TTFTC and DPNI ligands in the order …DAD…. Reprinted with permission from Ref 31 and 211. Copyright © 2015 Elsevier and Copyright © 2014 Royal Society of Chemistry.

a concomitant increase in conductivity (Fig. 15a).[39,209] Nie *et al.* subsequently extended the study to investigate TCNQ infiltration into other frameworks *via* computational methods, proposing up to ten materials to be promising for electrical conductivity.[210] On the other hand, in the system [(Zn(DMF))$_2$(TTFTC)(DPNI)] reported by Leong *et al.*,[31] through-space CT interactions were observed between the electron donor TTF and acceptor DPNI ligands by virtue of donor–acceptor interactions within its crystalline structure (Fig. 15b). This through-space interaction was manifested by the formation of ligand-based radicals in the as-synthesised material, and led to a control of the charge transfer *via* redox modulation.

Noncovalent host–guest interactions can also promote CT processes owing to the donor or acceptor nature of each moiety. Hybrid structures of electron-rich iodoplumbate nanowires precisely inserted into the periodic pores of electron-deficient pyridinium MOFs were recently reported by Liu *et al.* ($[K_5Zn_2(BCEBP)_3(OH)_2(H_2O)_2]_n[Pb_6I_{19}]_n$; space group: $P\bar{1}$).[204] In the MOF, the cationic host motif is based on zig-zag K–Zn–O ribbons, which are repeated by $K_5Zn_2O_{14}I_2$ clusters, whereas the guest motif is an infinite 1D iodoplumbate wire with a formula of $(Pb_6I_{19})_n^{3n-}$. Theoretical calculation demonstrated that the highest valence band of the hybrid material originated in the 1D iodoplumbate nanowires, while the lowest conduction band was contributed by the electron-deficient BCEBP linker. The composite was demonstrated as a narrow-bandgap semiconductor with a high and reversible photosensitivity. This represents the first example of a semiconducting MOF *in situ* loaded with inorganic semiconducting nanowires, as well as the first bicontinuous donor–acceptor hybrid at the molecular level based on host–guest interactions.

Finally, donor–acceptor interactions may also be exploited to engender molecular machineries. Li *et al.* reported a MOF constructed from struts in which donor–acceptor [2]catenane units became integrated, leading to a high density of these molecular machinery modules positioned precisely in well-defined layered (2D) structures.[212] This work constitutes a step towards the construction of new synthetic materials with dynamic behaviour for next-generation multifunctional MOF machineries.[167]

6.2. Mixed-valence systems

While donor and acceptor moieties usually present different identity, they may share the same nature but only differ in their formal oxidation states. In cases where the D and A units are equivalent, the phenomenon of mixed valency takes place. Such systems can be analysed within the Robin-Day classification scheme (Fig. 16).[213] The three primary Robin-Day classes correspond to: (i) two decoupled diabatic redox states and fully localised redox centres; (ii) moderate electronic coupling between the centres leading to a double-well adiabatic ground-state potential–energy curve with partly localised charges and a barrier for thermal electron transfer ET (the electronic coupling, $2H_{ab}$, is smaller than the Marcus reorganisation energy λ); and (iii) strong coupling with $2H_{ab} \geq \lambda$ leading to a single ground-state minimum without ET barrier (ΔG^*) and the charge being delocalised symmetrically between both redox centres. Most appealing is the design of class-II mixed-valence MOFs (Table 4), which will provide key information on charge transport inside 3D crystalline structures towards

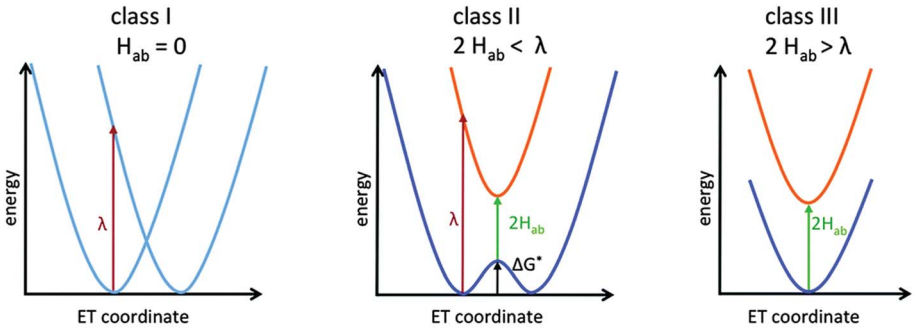

Fig. 16 Potential curves for the three primary Robin-Day classes of mixed-valence compounds. H_{ab}, λ and ΔG^* stand for electronic coupling, reorganisation energy, and free energy barrier, respectively.

understanding electron delocalisation in more complex biological and physical systems.

Metal-node mixed-valency. To date, mixed-valence mechanisms in MOFs with high intrinsic porosity have been suggested in a limited number of cases. However, exploiting the accessibility of metal atoms in several oxidation states is a promising strategy to design MOFs with improved redox properties. Fe(II/III) and Cu(I/II) are the most widely explored redox couples to engender mixed valency in MOFs, although other redox pairs have also been used. For example, Otsubo *et al.* reported the assembly of infinite square prism-shaped metal–organic nanotubes obtained from simple polymerization of a square-shaped metal–organic frame. The authors unambiguously demonstrated that one MX-chain of the MOF is in a Pt^{2+}/Pt^{4+} mixed valence charge-density wave state, thus opening the possibility of constructing new nanotubes with high designability through a bottom-up approach.[214]

Mixed-valence systems can be exemplified by Prussian blue, with formula $Fe_4^{III}[Fe^{II}(CN)_6]_3 \cdot xH_2O$, which has been used as a pigment since the early 17th century.[86,215] While not strictly a MOF, this framework comprises the donor and acceptor units Fe(II) and Fe(III), respectively, and exhibits intervalence CT (IVCT) processes between the D and A units. The material is a class-II mixed-valence compound,[90,215] in which the metal ions are weakly-coupled electronically leading to electron hopping between redox centres. The IVCT is mediated by CN-bridges (through-bond) and accounts for the semiconductor-type conductivity (5.5×10^{-5} S cm^{-1}) in this material.[216]

Fe-MIL-53·H_2O was arguably the first example of promoting mixed-valency in a MOF.[217] This hybrid material was used in an electrochemical cell, showing that uptake/removal of Li^+ ions accompanied with the reduction of Fe(III) into Fe(II) occurred reversibly during the charge/discharge process. Later, Yoon *et al.* examined the conditions for generating iron coordinatively unsaturated sites (CUS) with mixed valence Fe(II)/Fe(III) by activation of Fe-MIL-100,[91] and its consequences in gas sorption selectivity for potential environmental applications.[218] The reducibility of Fe-MIL-100 to form Fe(II) CUS was demonstrated to be essential for selective gas purification and selective removal of unsaturated gas impurities.

A series of Fe-MIL-53-type materials were prepared by Sun *et al.* with variable amounts of Fe^{2+} in the MOF.[219] Fe^{2+} and Fe^{3+} were demonstrated to coexist in the Fe(BDC)(DMF,F) framework. The diverse amount of Fe^{2+} in this series of Fe-MOFs allowed explain the distinction of reaction efficiency of phenol degradation with hydrogen peroxide as an oxidant at near neutral pH and 35 °C. Similarly, Benmansour *et al.* reported a series of honeycomb layered Fe(II)/Fe(III) mixed-valence MOFs with an eclipsed packing that generates hexagonal channels containing water inside.[220] The authors showed that it is possible to: (i) combine two cooperative properties such as electrical conductivity and magnetic ordering in a MOF thanks to the electron delocalisation provided by the mixed-valence character of the $[Fe(II)Fe(III)(C_6O_4X_2)_3]^-$ anionic lattice; (ii) modify the ordering temperature and electrical conductivity of these by changing the X group in the anilato ligand; and (iii) delaminate into nanosheets with thicknesses of a few layers and side dimensions of a few micrometers.

The strategy of redox matching between donor and acceptor components can be intelligently exploited to modulate CT, leading ultimately to charge transport enhancement. Dincă and co-workers demonstrated the importance of mixed valency in achieving electrical conductivity in the series M_2(DSBDC) (M = Mn(II) and Fe(II)).[30,207,221] Substitution of O in DOBDC for S in DSBDC as the donor atom resulted in an order of magnitude increase in conductivity, from 3.0×10^{-13} to 1.2×10^{-12} S cm^{-1} for the Mn(II) analogue and from 4.6×10^{-8} to 5.8×10^{-7} S cm^{-1} for the Fe(II) analogue.[207] Infinite Mn–S chains found within the framework were proposed to serve as conduction pathways. Further extension of this work was carried out by Sun *et al.* reporting four isostructural series of MOFs with formulas $[M_2(DOBDC)(DMF)_2]$ (M = Mg^{2+}, Mn^{2+}, Fe^{2+}, Co^{2+}, Ni^{2+}, Cu^{2+}, Zn^{2+}), $[M_2(DSBDC)(DMF)_2]$ (M = Mn^{2+}, Fe^{2+}), $[M_2Cl_2(BTDD)\text{-}(DMF)_2]$ (M = Mn^{2+}, Fe^{2+}, Co^{2+}, Ni^{2+}), and $[M(TRI)_2]$ (M = Mg^{2+}, Mn^{2+}, Fe^{2+}, Co^{2+}, Cu^{2+}, Zn^{2+}, Cd^{2+}).[30] The Fe analogues were found to exhibit significantly higher conductivities and lower activation energies in comparison to the other first-row transition metals (Fig. 17a). The authors attributed the unique electrical properties of iron-based MOFs to the high-energy valence electrons of Fe^{2+} and the $Fe^{3+/2+}$ mixed valency formation.

Introducing mixed-valency towards oxidation of Fe(II/III)-based MOFs has demonstrated a powerful strategy for inducing electrical conductivity up to S cm^{-1} units in 3D hybrid

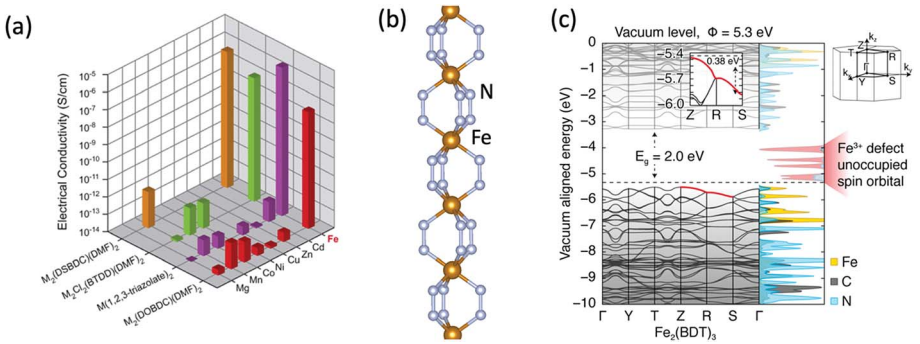

Fig. 17 (a) Electrical conductivity in $M_2(DOBDC)(DMF)_2$, $M_2(DSBDC)(DMF)_2$, $M_2Cl_2(BTDD)(DMF)_2$, and $M(TRI)_2$ measured at 300 K, in N_2 atmosphere, and in the dark. (b) $(Fe–N–N–)_\infty$ chains, which serve as the presumed charge transport pathway in $Fe_2(BDP)_3$ and $Fe_2(BDT)_3$. (c) Calculated band structure and density of states for partially oxidized $Fe_2(BDT)_3$, modelled as a framework in which 1/8 of the Fe^{2+} sites are replaced with Fe^{3+}. Reprinted with permission from ref. 11 and 30. Copyright © 2017 Royal Society of Chemistry and Copyright © 2018 American Chemical Society.

materials. Park *et al.* have just reported the $Fe(TRI)_2(BF_4)_x$ framework through stoichiometric chemical oxidation of $Fe(TRI)_2$.[10] Interestingly, the most oxidized variant $Fe(TRI)_2(BF_4)_{0.33}$ displayed a conductivity of 0.3 S cm^{-1} at room temperature. The high electronic conductivities are linked to the high degree of charge delocalisation between octahedral low-spin Fe(II) and Fe(III) centres. Similarly, Aubrey *et al.* have reported a Fe(III)-based MOF ($Fe_2(BDP)_3$ with *Fddd* space group) that can be partially reduced ($K_xFe_2(BDP)_3$ with $0 \leq x \leq 2$) leading to a 10 000-hold conductivity enhancement up to 0.025 S cm^{-1}.[208] The authors demonstrated that the structural motif $[Fe(pyrazole)_3]_\infty$ comprised of 1D-like Fe-based chains (Fig. 17b) is an ideal precursor to achieve porous Fe(II/III) mixed-valence materials with high charge mobilities through sub-stoichiometric chemical reduction. Finally, Xie *et al.* have recently reported the highest single crystal conductivity of 1.8 S cm^{-1} in a 3D MOF of Fe(II)-based nodes and benzene ditetrazole (BDT) linkers.[11] The $Fe_2(BDT)_3$ MOF (space group: *Cmmm*), containing the $(Fe–N–N–)_\infty$ chains (Fig. 17b), yields a mixed-valence material upon exposure to ambient atmosphere, and offers tuneable conductivities over five orders of magnitude due to the introduction of low-lying Fe^{3+} defect states in the bandgap region (Fig. 17c). Incorporating Fe^{2+}/Fe^{3+} in the charge transport pathways of MOFs and promoting partial oxidation/reduction to engender mixed valency is therefore an innovative strategy for improving charge transport in this emerging class of conducting porous materials.

Although Fe(II/III) mixed valency has captured the majority of attention, other systems such as Cu(I/II/III) have also been subject of intensive research toward the generation of mixed-valence MOFs.[222–224] Mixed valency has been claimed as the origin of conductivity in the $Cu[Cu(PDT)_2]$ material reported by Takaishi *et al.*, which contains the donor Cu(I) and acceptor $[Cu(III)(PDT)_2]^-$ units.[205] The reasonably high conductivity of 6×10^{-4} S cm^{-1} at 300 K was attributed to the bistability of mixed-valence $Cu(I)[Cu(III)(PDT)_2]$ and $Cu(II)[Cu(II)(PDT)_2]$ states, with the appearance of a low-lying IVCT band in the infrared spectrum of $Cu[Cu(PDT)_2]$.

Guest intercalation as a strategy to induce mixed valency has also been explored. The heterometallic framework $Cu[Ni(PDT)_2]$ presents a significantly lower conductivity (1×10^{-8} S cm^{-1}) compared to its isostructural $Cu[Cu(PDT)_2]$ analogue,[205] consistent with its larger optical bandgap.[205] The Kobayashi *et al.* however demonstrated that this heterometallic MOF can be partially oxidized with iodine to yield a p-type semiconductor with a 4-fold increase in the conductivity (1×10^{-4} S cm^{-1}),[206] whose oxidation process was unambiguously ascribed to Ni-based node-centred electron extraction.

Mixed-valence ligands. Introduction of mixed-valency through ligands is another interesting strategy to promote redox activity in MOFs that has received attention recently. Although less common than metal-based mixed-valency, several organic linkers may exhibit dual oxidation states owing to the formation of relatively stable radical species.

A series of hydrophobic POPs containing redox-active triarylamines linked by ethynyl (POP-1), 1,4-diethynylphenyl (POP-2) and 4,4′-diethynylbiphenyl (POP-3) bridges were synthesised and characterised by Hua *et al.*[225] The facile electrochemical or chemical oxidation of the POPs generated mixed-valence radical cation states with markedly enhanced adsorption properties relative to their neutral analogues, including a 3-fold improvement in the H_2 uptake at 77 K and 1 bar, and an increase in the isosteric heat of adsorption for CO_2.

Overall, the transition metal–semiquinoid system is established as a particularly promising moiety to achieving tuneable long-range electronic communication in MOFs.[226] An interesting example was recently reported in the framework $[(TBA)_2Fe_2^{III}(DHBQ)_3]$ (Fig. 18).[49] Here, the ligands are present in both their quinone and semiquinone forms $(DHBQ)^{2-/3-}$, giving rise to an IVCT transition. Importantly, UV-vis-NIR diffuse reflectance measurements revealed for this material the first observation of Class II/III mixed valency in a MOF. Chemical reduction of the MOF to $Na_{0.9}[(TBA)_{1.8}Fe_2(DHBQ)_3]$ produced increased radical $(DHBQ)^{3-}$ species, resulting in a lowering in the intensity of the IVCT band, as well as a decrease in the conductivity (from 0.16 to 0.0062 S cm^{-1}). Later, the isostructural $(H_2NMe_2)_2M_2(Cl_2DHBQ)_3$ (M = Ti, V)

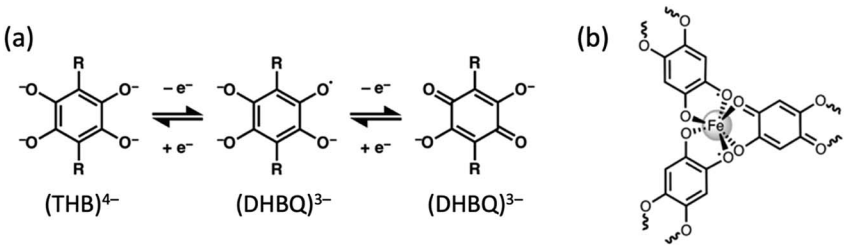

Fig. 18 (a) Redox states of linkers deriving from 2,5-dihydroxybenzo-quinone. (b) Illustration of a single Fe^{III} center in $[(TBA)_2Fe_2^{III}(DHBQ)_3]$, showing that two radical $(DHBQ)^{3-}$ bridging ligands and one diamagnetic $DHBQ^{2-}$ bridging ligand are coordinated to each metal site.

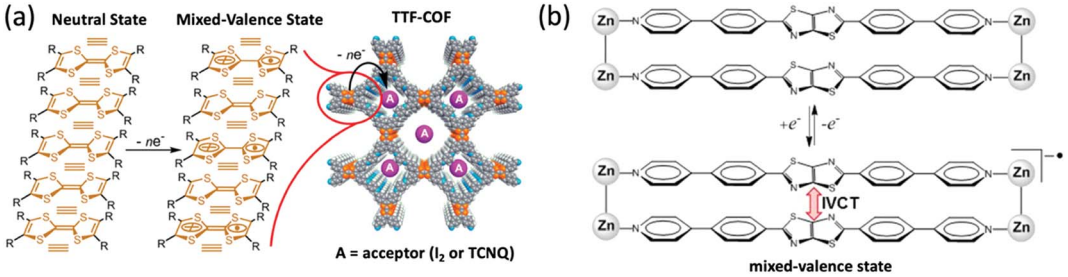

Fig. 19 (a) Illustration of the mixed-valence state in TTF-COF. The "≡" indicates inter-TTF-layer interactions. (b) Schematic representation of the cofacial pair of BPPTzTz ligands showing reduction to the mixed-valence state which facilitates a through-space IVCT interaction. Reprinted with permission from ref. 44 and 232. Copyright © 2014 Royal Society of Chemistry and Copyright © 2018 American Chemical Society.

and $(H_2NMe_2)_{1.5}Cr_2(DHBQ)_3$ showed to exhibit substantial differences in their electronic structures, with a direct correlation between the bulk conductivity and the extent of charge delocalization. The authors could correlate the metal–ligand energy alignment with the energy of intervalence charge-transfer transitions, which in turn should determine the charge hopping barrier in mixed-valence MOFs.[227]

The electron rich TTF unit is well-known to promote mixed valency in organic derivatives when attached through-bond to electron-acceptor moieties[228,229] or when self-stacked through space by means of noncovalent interactions.[230,231] Tetrathiafulvalene moieties were found to coexist in a mixed-valence state in a *de novo* purely-organic framework reported by Cai *et al.*[232] The TTF-COF was demonstrated to be semiconductor with the existence of intermolecular TTF-centred charge-transfer processes. Upon I_2 doping of this material, the conductivity increased 3 orders of magnitude as a result of optimizing the degree of charge transfer in the TTF stacks (Fig. 19a). Otherwise, Chen *et al.* characterized a 3D MOF constructed from tetranuclear cluster nodes built through the μ^2-O bridge of the TTF ligand, which was first found for TTF coordination polymers.[132] The authors demonstrated that the channel generated by the 3D MOF exerts a confinement effect on the formation of TTF dimers. The TTF dimers showed strong intradimer interaction with partial charge transfer, thus providing good photocurrent response.

It has recently been demonstrated that aromatic stacking interactions in Zn(II) frameworks containing cofacial thiazolo [5,4-*d*]thiazole units lead to a mixed-valence state upon electrochemical or chemical reduction (Fig. 19b).[44] Hua *et al.* synthesized a Zn(II)-based MOF that crystallizes in the orthorhombic space group *Pcc*2, containing BPPTzTz ligands and TDC coligands. Importantly, the TDC coligand holds two π-stacking BPPTzTz ligands in close proximity (ligand-to-ligand distance of 3.80 Å), which eventually lead to an intervalence (one-electron) charge transfer (IVCT) from one moiety to the other after (electro)chemical reduction. This through-space IVCT phenomenon represents a new mechanism for charge transfer in MOFs, and provides insight to better understand charge transport in more complex biological such as bacterial photosynthesis. Elaboration of this through-space mixed-valence interaction could also lead to long-range delocalization, essential for enhancing conductivity.

7. Conclusions

Promotion of redox activity in metal–organic frameworks represents an appealing strategy to boost the utility of hybrid frameworks in fields that extend beyond their traditional application areas of gas storage and separation. We have reviewed the most recent strategies and successes in installing redox activity in MOFs, relating the new properties upon electroactivation to emerging application areas in energy conversion and storage. Redox-tunability of metal-based nodes in MOFs has consolidated as a potential strategy towards single-site selective sorption and multi-electron redox catalysis. Otherwise, the uncountable opportunities to fine-tune the structural and electronic properties of MOFs by introducing and modifying novel organic linkers and guest molecules/nanoparticles has already offered insight into unconventional

catalytic reactivity and complex redox phenomena. Incorporation of mixed-valency into MOFs has become one of the most successful approaches to better understand the electron transfer processes in three-dimensional networks, while improving the carrier transport, including the first reports of metallic hybrid frameworks. A significant synergistic work between theoreticians and experimentalists is however required in the near future to elucidate the mechanisms of charge transport and to further enhance the conductivity in the framework. As long as MOFs achieve high charge transport properties, novel and unexplored areas of application for these materials will be unlocked, permeating into disciplines as varied as electronics, sensing, optics and photovoltaics.

Conflicts of interest

There are no conflicts to declare.

Abbreviations

AQDC	2,7-Anthraquinonedicarboxylate
BCEBP	*N*,*N*′-Bis(carboxyethyl)-4,4′-bipyridinium
BDC	Benzene-1,4-dicarboxylate
BDT	5,5′-(1,4-Phenylene)bis(1*H*-tetrazole)
BHT	Benzenehexathiol
BDP	Benzenedipyrazolate
BP	4,4′-Bipyridine
BPDC	4,4′-Biphenyl dicarboxylate
BPDPNDI	*N*,*N*′-Bis(4-pyridyl)-2,6-dipyrrolidyl naphthalenediimide
BPNDI	*N*,*N*′-Di(4-pyridyl)-1,4,5,8-naphthalenediimide
BPPTzTz	4,4′-Dipyridyl-thiazolothiazole
BPyDC	2,2′-Bipyridine-5,5′-dicarboxylate
BTC	Benzene 1,3,5-tricarboxylate
BTDD	Bis(1,2,3-triazolato-[4,5-*b*],[4′,5′-*i*])dibenzo-[1,4]-dioxin
DCDHBQ	2,5-Dichloro-3,6-dihydroxo-1,4-benzoquinone
DHBDC	2,3-Dihydroxy-1,4-benzenedicarboxylate
DHBQ	3,6-Dihydroxo-1,4-benzoquinone
DMF	Dimethylformamide
DMDPB	1,4-Bis(3,5-dimethyl)dipyrazol-4-ylbenzene
DPMBI	*N*,*N*′-Di-(4-pyridylmethyl)-1,2,4,5-benzenetetracarboxydiimide
DPNI	*N*,*N*′-Di(4-pyridyl)-1,4,5,8-naphthalenetetracarboxydiimide
DOBDC	2,5-Dihydroxybenzene-1,4-dicarboxylate
DSBDC	2,5-Disulfhydrylbenzene-1,4-dicarboxylate
FDMS	1,1′-Ferrocenediyl-dimethylsilane
HFIPBB	4,4′-(Hexafluoroisopropylidene)bisbenzoate
HITP	2,3,6,7,10,11-Hexaiminotriphenylene
NDC	2,7-Naphthalene dicarboxylate
NDI	Naphtalenediimide
NDISA	Naphthalene diimide salicylic acid
PBDA	3-(Pyridine-3-yloxy)benzene-1,2-dicarboxylate
PDT	2,3-Pyrazine dithiolate
TBA	Tetrabutylammonium
TBAP	1,3,6,8-Tetrakis(*p*-benzoate)pyrene
TBSIB	*tert*-Butylsulfonyl-2-iodosylbenzene
TCA	Tricarboxytriphenylamine
TCNQ	Tetracyanoquinodimethane
TCPP	Tetrakis(4-carboxyphenyl)porphyrin
TDC	2,5-Thiophene dicarboxylic acid
TEMPO	2,2,6,6-Tetramethyl-1-piperidinyloxy
THB	1,2,4,5-Tetrahydroxobenzene
TP	2,2′:6′,2″-Terpyridine
TPPA	Tris(4-(pyridin-4-yl)phenyl)amine
TRI	1,2,3-Triazolate
TTF	Tetrathiafulvalene
TTFTB	Tetrathiafulvalene tetrabenzoate
TTFTC	Tetrathiafulvalene tetracarboxylate
TTFTP	Tetra(4-pyridyl)tetrathiafulvalene

Acknowledgements

This project was supported by the Generalitat Valenciana postdoctoral APOSTD/2017/081 fellowship, and the Royal Society University Research Fellowship Scheme. This research was also supported by the Creative Materials Discovery Program through the National Research Foundation of Korea (NRF) funded by Ministry of Science and ICT (2018M3D1A1058536).

References

1 O. M. Yaghi, H. Li, M. Eddaoudi and M. O'Keeffe, *Nature*, 1999, **402**, 276–279.
2 S. R. Batten, S. M. Neville and D. R. Turner, *Coordination Polymers*, Royal Society of Chemistry, Cambridge, 2008.
3 L. Jiao, Y. Wang, H.-L. Jiang and Q. Xu, *Adv. Mater.*, 2017, 1703663.
4 G. Mínguez Espallargas and E. Coronado, *Chem. Soc. Rev.*, 2018, **47**, 533–557.
5 R. Medishetty, J. K. Zaręba, D. Mayer, M. Samoć and R. A. Fischer, *Chem. Soc. Rev.*, 2017, **46**, 4976–5004.
6 J. Hao, X. Xu, H. Fei, L. Li and B. Yan, *Adv. Mater.*, 2018, **30**, 1705634.
7 D. Feng, T. Lei, M. R. Lukatskaya, J. Park, Z. Huang, M. Lee, L. Shaw, S. Chen, A. A. Yakovenko, A. Kulkarni, J. Xiao, K. Fredrickson, J. B. Tok, X. Zou, Y. Cui and Z. Bao, *Nat. Energy*, 2018, **3**, 30–36.
8 L. Sun, M. G. Campbell and M. Dincă, *Angew. Chem., Int. Ed.*, 2016, **55**, 3566–3579.
9 L. Sun, C. H. Hendon, S. S. Park, Y. Tulchinsky, R. Wan, F. Wang, A. Walsh and M. Dincă, *Chem. Sci.*, 2017, **8**, 4450–4457.
10 J. G. Park, M. L. Aubrey, J. Oktawiec, K. Chakarawet, L. E. Darago, F. Grandjean, G. J. Long and J. R. Long, *J. Am. Chem. Soc.*, 2018, **140**, 8526–8534.
11 L. S. Xie, L. Sun, R. Wan, S. S. Park, J. A. DeGayner, C. H. Hendon and M. Dincă, *J. Am. Chem. Soc.*, 2018, **140**, 7411–7414.
12 Y. Ren, G. H. Chia and Z. Gao, *Nano Today*, 2013, **8**, 577–597.

13 G. Xu, P. Nie, H. Dou, B. Ding, L. Li and X. Zhang, *Mater. Today*, 2017, **20**, 191–209.
14 A. A. Talin, R. E. Jones and P. E. Hopkins, *MRS Bull.*, 2016, **41**, 877–882.
15 K. J. Erickson, F. Léonard, V. Stavila, M. E. Foster, C. D. Spataru, R. E. Jones, B. M. Foley, P. E. Hopkins, M. D. Allendorf and A. A. Talin, *Adv. Mater.*, 2015, **27**, 3453–3459.
16 L. Liu, Y. Zhou, S. Liu and M. Xu, *ChemElectroChem*, 2018, **5**, 6–19.
17 D. M. D'Alessandro, *Chem. Commun.*, 2016, **52**, 8957–8971.
18 H. Wang, Q.-L. Zhu, R. Zou and Q. Xu, *Chem*, 2017, **2**, 52–80.
19 L. Sun, M. G. Campbell and M. Dincă, *Angew. Chem., Int. Ed.*, 2016, **55**, 3566–3579.
20 Y. Zhang, S. N. Riduan and J. Wang, *Chem.–Eur. J.*, 2017, **23**, 16419–16431.
21 H. Bin Wu and X. W. (David) Lou, *Sci. Adv.*, 2017, **3**, eaap9252.
22 Z. Zhang and K. Awaga, *MRS Bull.*, 2016, **41**, 883–889.
23 M. B. Solomon, T. L. Church and D. M. D'Alessandro, *CrystEngComm*, 2017, **19**, 4049–4065.
24 C. H. Hendon, A. J. Rieth, M. D. Korzyński and M. Dincă, *ACS Cent. Sci.*, 2017, **3**, 554–563.
25 B. Gui, Y. Meng, Y. Xie, K. Du, A. C.-H. Sue and C. Wang, *Macromol. Rapid Commun.*, 2018, **39**, 1700388.
26 C. L. Jones, A. J. Tansell and T. L. Easun, *J. Mater. Chem. A*, 2016, **4**, 6714–6723.
27 Y. Tulchinsky, C. H. Hendon, K. A. Lomachenko, E. Borfecchia, B. C. Melot, M. R. Hudson, J. D. Tarver, M. D. Korzyński, A. W. Stubbs, J. J. Kagan, C. Lamberti, C. M. Brown and M. Dincă, *J. Am. Chem. Soc.*, 2017, **139**, 5992–5997.
28 D. Shi, R. Zheng, M.-J. Sun, X. Cao, C.-X. Sun, C.-J. Cui, C.-S. Liu, J. Zhao and M. Du, *Angew. Chem., Int. Ed.*, 2017, **56**, 14637–14641.
29 N. S. Lopa, M. M. Rahman, F. Ahmed, S. C. Sutradhar, T. Ryu and W. Kim, *J. Electroanal. Chem.*, 2018, **822**, 43–49.
30 L. Sun, C. H. Hendon, S. S. Park, Y. Tulchinsky, R. Wan, F. Wang, A. Walsh and M. Dincă, *Chem. Sci.*, 2017, **8**, 4450–4457.
31 C. F. Leong, B. Chan, T. B. Faust and D. M. D'Alessandro, *Chem. Sci.*, 2014, **5**, 4724–4728.
32 Z. Guo, D. K. Panda, M. A. Gordillo, A. Khatun, H. Wu, W. Zhou and S. Saha, *ACS Appl. Mater. Interfaces*, 2017, **9**, 32413–32417.
33 S. S. Park, E. R. Hontz, L. Sun, C. H. Hendon, A. Walsh, T. Van Voorhis and M. Dincă, *J. Am. Chem. Soc.*, 2015, **137**, 1774–1777.
34 C. K. Brozek and M. Dincă, *J. Am. Chem. Soc.*, 2013, **135**, 12886–12891.
35 M. Kim, J. F. Cahill, H. Fei, K. A. Prather and S. M. Cohen, *J. Am. Chem. Soc.*, 2012, **134**, 18082–18088.
36 N. Sikdar, K. Jayaramulu, V. Kiran, K. V. Rao, S. Sampath, S. J. George and T. K. Maji, *Chem.–Eur. J.*, 2015, **21**, 11701–11706.
37 A. Van Wyk, T. Smith, J. Park and P. Deria, *J. Am. Chem. Soc.*, 2018, **140**, 2756–2760.
38 I. Hod, O. K. Farha and J. T. Hupp, *Chem. Commun.*, 2016, **52**, 1705–1708.
39 A. A. Talin, A. Centrone, A. C. Ford, M. E. Foster, V. Stavila, P. Haney, R. A. Kinney, V. Szalai, F. El Gabaly, H. P. Yoon, F. Léonard and M. D. Allendorf, *Science*, 2013, **343**, 66–69.
40 T. Kambe, R. Sakamoto, T. Kusamoto, T. Pal, N. Fukui, K. Hoshiko, T. Shimojima, Z. Wang, T. Hirahara, K. Ishizaka, S. Hasegawa, F. Liu and H. Nishihara, *J. Am. Chem. Soc.*, 2014, **136**, 14357–14360.
41 J.-H. Dou, L. Sun, Y. Ge, W. Li, C. H. Hendon, J. Li, S. Gul, J. Yano, E. A. Stach and M. Dincă, *J. Am. Chem. Soc.*, 2017, **139**, 13608–13611.
42 M. Ko, L. Mendecki and K. A. Mirica, *Chem. Commun.*, 2018, **54**, 7873–7891.
43 T. C. Narayan, T. Miyakai, S. Seki and M. Dincă, *J. Am. Chem. Soc.*, 2012, **134**, 12932–12935.
44 C. Hua, P. W. Doheny, B. Ding, B. Chan, M. Yu, C. J. Kepert, D. M. D 'alessandro and P. W. Doheny, *J. Am. Chem. Soc.*, 2018, **140**, 6622–6630.
45 J. E. Halls, D. Jiang, A. D. Burrows, M. A. Kulandainathan and F. Marken, in *Electrochemistry*, 2013, vol. 12, pp. 187–210.
46 A. Doménech-Carbó, *Electrochemistry of porous materials*, CRC Press, Boca Raton, Florida, 2010.
47 I. Hod, W. Bury, D. M. Gardner, P. Deria, V. Roznyatovskiy, M. R. Wasielewski, O. K. Farha and J. T. Hupp, *J. Phys. Chem. Lett.*, 2015, **6**, 586–591.
48 S. R. Ahrenholtz, C. C. Epley and A. J. Morris, *J. Am. Chem. Soc.*, 2014, **136**, 2464–2472.
49 L. E. Darago, M. L. Aubrey, C. J. Yu, M. I. Gonzalez and J. R. Long, *J. Am. Chem. Soc.*, 2015, **137**, 15703–15711.
50 P. M. Usov, C. Fabian and D. M. D'Alessandro, *Chem. Commun.*, 2012, **48**, 3945.
51 C. R. Wade, M. Li and M. Dincă, *Angew. Chem., Int. Ed.*, 2013, **52**, 13377–13381.
52 F. J. Rizzuto, T. B. Faust, B. Chan, C. Hua, D. M. D'Alessandro and C. J. Kepert, *Chem.–Eur. J.*, 2014, **20**, 17597–17605.
53 C. Hua and D. M. D'Alessandro, *CrystEngComm*, 2014, **16**, 6331–6334.
54 C. Hua, P. Turner and D. M. D'Alessandro, *Dalton Trans.*, 2013, **42**, 6310.
55 F.-X. Coudert and A. H. Fuchs, *Coord. Chem. Rev.*, 2016, **307**, 211–236.
56 K. Lejaeghere, G. Bihlmayer, T. Björkman, P. Blaha, S. Blügel, V. Blum, D. Caliste, I. E. Castelli, S. J. Clark, A. Dal Corso, S. de Gironcoli, T. Deutsch, J. K. Dewhurst, I. Di Marco, C. Draxl, M. Dułak, O. Eriksson, J. A. Flores-Livas, K. F. Garrity, L. Genovese, P. Giannozzi, M. Giantomassi, S. Goedecker, X. Gonze, O. Grånäs, E. K. U. Gross, A. Gulans, F. Gygi, D. R. Hamann, P. J. Hasnip, N. A. W. Holzwarth, D. Iuşan, D. B. Jochym, F. Jollet, D. Jones, G. Kresse, K. Koepernik, E. Küçükbenli, Y. O. Kvashnin, I. L. M. Locht, S. Lubeck, M. Marsman, N. Marzari, U. Nitzsche, L. Nordström, T. Ozaki, L. Paulatto, C. J. Pickard, W. Poelmans, M. I. J. Probert, K. Refson, M. Richter, G.-M. Rignanese, S. Saha,

M. Scheffler, M. Schlipf, K. Schwarz, S. Sharma, F. Tavazza, P. Thunström, A. Tkatchenko, M. Torrent, D. Vanderbilt, M. J. van Setten, V. Van Speybroeck, J. M. Wills, J. R. Yates, G.-X. Zhang and S. Cottenier, *Science*, 2016, **351**, aad3000.

57 L. Protesescu, S. Yakunin, M. I. Bodnarchuk, F. Krieg, R. Caputo, C. H. Hendon, R. X. Yang, A. Walsh and M. V. Kovalenko, *Nano Lett.*, 2015, **15**, 3692–3696.

58 X. Nie, A. Kulkarni and D. S. Sholl, *J. Phys. Chem. Lett.*, 2015, **6**, 1586–1591.

59 J. Jelic, D. Denysenko, D. Volkmer and K. Reuter, *New J. Phys.*, 2013, **15**, 115004.

60 A. J. Clough, J. M. Skelton, C. A. Downes, A. A. de la Rosa, J. W. Yoo, A. Walsh, B. C. Melot and S. C. Marinescu, *J. Am. Chem. Soc.*, 2017, **139**, 10863–10867.

61 S. Grimme, J. Antony, S. Ehrlich and H. Krieg, *J. Chem. Phys.*, 2010, **132**, 154104.

62 O. A. Vydrov and T. Van Voorhis, *Phys. Rev. Lett.*, 2009, **103**, 063004.

63 J. Calbo, E. Ortí, J. C. Sancho-García and J. Aragó, *Annu. Rep. Comput. Chem.*, 2015, **11**, 37–102.

64 R. B. Getman, Y.-S. Bae, C. E. Wilmer and R. Q. Snurr, *Chem. Rev.*, 2012, **112**, 703–723.

65 L. Ye, J. Liu, Y. Gao, C. Gong, M. Addicoat, T. Heine, C. Wöll and L. Sun, *J. Mater. Chem. A*, 2016, **4**, 15320–15326.

66 M. Dan-Hardi, C. Serre, T. Frot, L. Rozes, G. Maurin, C. Sanchez, G. Férey and G. Maurín, *J. Am. Chem. Soc.*, 2009, **131**, 10857–10859.

67 Z. Lu, H. G. W. Godfrey, I. Da Silva, Y. Cheng, M. Savage, F. Tuna, E. J. L. McInnes, S. J. Teat, K. J. Gagnon, M. D. Frogley, P. Manuel, S. Rudić, A. J. Ramirez-Cuesta, T. L. Easun, S. Yang and M. Schröder, *Nat. Commun.*, 2017, **8**, 14212.

68 M. K. Leszczyński, A. Kornowicz, D. Prochowicz, I. Justyniak and K. Noworyta, *Inorg. Chem.*, 2018, **57**, 4803–4806.

69 A. W. Stubbs, L. Braglia, E. Borfecchia, R. J. Meyer, Y. Román-Leshkov, C. Lamberti and M. Dincă, *ACS Catal.*, 2018, **8**, 596–601.

70 C. K. Brozek, J. T. Miller, S. A. Stoian and M. Dincă, *J. Am. Chem. Soc.*, 2015, **137**, 7495–7501.

71 X. Wang, X. Liu, H. Rong, Y. Song, H. Wen and Q. Liu, *RSC Adv.*, 2017, **7**, 29611–29617.

72 E. D. Bloch, L. J. Murray, W. L. Queen, S. Chavan, S. N. Maximoff, J. P. Bigi, R. Krishna, V. K. Peterson, F. Grandjean, G. J. Long, B. Smit, S. Bordiga, C. M. Brown and J. R. Long, *J. Am. Chem. Soc.*, 2011, **133**, 14814–14822.

73 D. J. Xiao, E. D. Bloch, J. A. Mason, W. L. Queen, M. R. Hudson, N. Planas, J. Borycz, A. L. Dzubak, P. Verma, K. Lee, F. Bonino, V. Crocellà, J. Yano, S. Bordiga, D. G. Truhlar, L. Gagliardi, C. M. Brown and J. R. Long, *Nat. Chem.*, 2014, **6**, 590–595.

74 E. D. Bloch, W. L. Queen, S. Chavan, P. S. Wheatley, J. M. Zadrozny, R. Morris, C. M. Brown, C. Lamberti, S. Bordiga and J. R. Long, *J. Am. Chem. Soc.*, 2015, **137**, 3466–3469.

75 L. Yang, C. Xu, W. Ye and W. Liu, *Sens. Actuators, B*, 2015, **215**, 489–496.

76 Z. Zhang, H. Yoshikawa and K. Awaga, *J. Am. Chem. Soc.*, 2014, **136**, 16112–16115.

77 D. Zhang, J. Zhang, R. Zhang, H. Shi, Y. Guo, X. Guo, S. Li and B. Yuan, *Talanta*, 2015, **144**, 1176–1181.

78 D. Yue, D. Zhao, J. Zhang, L. Zhang, K. Jiang, X. Zhang, Y. Cui, Y. Yang, B. Chen and G. Qian, *Chem. Commun.*, 2017, **53**, 11221–11224.

79 S. Yuan, J.-S. Qin, C. T. Lollar and H.-C. Zhou, *ACS Cent. Sci.*, 2018, **4**, 440–450.

80 A. Walsh and C. R. A. Catlow, *ChemPhysChem*, 2010, **11**, 2341–2344.

81 C. H. Hendon, D. Tiana, M. Fontecave, C. Sanchez, L. D'Arras, C. Sassoye, L. Rozes, C. Mellot-Draznieks and A. Walsh, *J. Am. Chem. Soc.*, 2013, **135**, 10942–10945.

82 H. L. Nguyen, F. Gándara, H. Furukawa, T. L. H. Doan, K. E. Cordova and O. M. Yaghi, *J. Am. Chem. Soc.*, 2016, **138**, 4330–4333.

83 P. Van Der Voort, K. Leus, Y.-Y. Liu, M. Vandichel, V. Van Speybroeck, M. Waroquier and S. Biswas, *New J. Chem.*, 2014, **38**, 1853–1867.

84 Z. Lu, H. G. W. Godfrey, I. da Silva, Y. Cheng, M. Savage, P. Manuel, S. Rudić, A. J. Ramirez-Cuesta, S. Yang and M. Schröder, *Chem. Sci.*, 2018, **9**, 3401–3408.

85 D. Kolb, *J. Chem. Educ.*, 1988, **65**, 1004.

86 A. Ludi, *J. Chem. Educ.*, 1981, **58**, 1013.

87 H. J. Emeléus and A. G. Sharpe, *Advances in inorganic chemistry and radiochemistry*, Academic Press, London, 1962, vol. 4.

88 B. Kong, C. Selomulya, G. Zheng and D. Zhao, *Chem. Soc. Rev.*, 2015, **44**, 7997–8018.

89 D. Maspoch, D. Ruiz-Molina and J. Veciana, *Chem. Soc. Rev.*, 2007, **36**, 770.

90 A. A. Karyakin, *Electroanalysis*, 2001, **13**, 813–819.

91 P. Horcajada, S. Surblé, C. Serre, D.-Y. Hong, Y.-K. Seo, J.-S. Chang, J.-M. Grenèche, I. Margiolaki and G. Férey, *Chem. Commun.*, 2007, **100**, 2820–2822.

92 A. R. Kim, T. U. Yoon, E. J. Kim, J. W. Yoon, S. Y. Kim, J. W. Yoon, Y. K. Hwang, J. S. Chang and Y. S. Bae, *Chem. Eng. J.*, 2018, **331**, 777–784.

93 D. J. Xiao, J. Oktawiec, P. J. Milner and J. R. Long, *J. Am. Chem. Soc.*, 2016, **138**, 14371–14379.

94 T. Zhang, Y.-Q. Hu, T. Han, Y.-Q. Zhai and Y.-Z. Zheng, *ACS Appl. Mater. Interfaces*, 2018, **10**, 15786–15792.

95 S. Z. Tasker, E. A. Standley and T. F. Jamison, *Nature*, 2014, **509**, 299–309.

96 H. R. Moon, J. H. Kim and M. P. Suh, *Angew. Chem., Int. Ed.*, 2005, **44**, 1261–1265.

97 D. Sheberla, L. Sun, M. A. Blood-Forsythe, S. Er, C. R. Wade, C. K. Brozek, A. Aspuru-Guzik and M. Dincă, *J. Am. Chem. Soc.*, 2014, **136**, 8859–8862.

98 E. M. Miner, T. Fukushima, D. Sheberla, L. Sun, Y. Surendranath and M. Dincă, *Nat. Commun.*, 2016, **7**, 10942.

99 J. K. Burdett and S. Sevov, *J. Am. Chem. Soc.*, 1995, **117**, 12788–12792.

100 Q. Fu, K. Xie, S. Tan, J. M. Ren, Q. Zhao, P. A. Webley and G. G. Qiao, *Chem. Commun.*, 2016, **52**, 12226–12229.

101 C. Pagis, M. Ferbinteanu, G. Rothenberg and S. Tanase, *ACS Catal.*, 2016, **6**, 6063–6072.
102 S. Fordham, X. Wang, M. Bosch and H.-C. Zhou, in *Lanthanide Metal-Organic Frameworks*, Springer Berlin Heidelberg, Berlin, 2014, pp. 1–27.
103 S. Smolders, K. A. Lomachenko, B. Bueken, A. Struyf, A. L. Bugaev, C. Atzori, N. Stock, C. Lamberti, M. B. J. Roeffaers and D. E. De Vos, *ChemPhysChem*, 2018, **19**, 373–378.
104 D. M. D'Alessandro, *Chem. Commun.*, 2016, **52**, 8957–8971.
105 E. M. Miner, S. Gul, N. D. Ricke, E. Pastor, J. Yano, V. K. Yachandra, T. Van Voorhis and M. Dincă, *ACS Catal.*, 2017, **7**, 7726–7731.
106 K. L. Mulfort and J. T. Hupp, *J. Am. Chem. Soc.*, 2007, **129**, 9604–9605.
107 C. R. Wade, M. Li and M. Dinca, *Angew. Chem., Int. Ed.*, 2013, **52**, 13377–13381.
108 Z. Peng, X. Yi, Z. Liu, J. Shang and D. Wang, *ACS Appl. Mater. Interfaces*, 2016, **8**, 14578–14585.
109 M. Souto, A. Santiago-Portillo, M. Palomino, I. Vitorica-Yrzebal, B. J. C. Vieira, J. C. C. Waerenborgh, S. Valencia, S. Navalon, F. Rey, H. Garcia and G. Minguez Espallargas, *Chem. Sci.*, 2018, **9**, 2413–2418.
110 M. Souto, J. Romero, J. Calbo, I. J. Vitorica-Yrezabal, J. L. Zafra, J. Casado Cordón, E. Ortí, A. Walsh and G. Minguez Espallargas, *J. Am. Chem. Soc.*, 2018, **140**, 10562–10569.
111 A. F. Cozzolino, C. K. Brozek, R. D. Palmer, J. Yano, M. Li and M. Dincă, *J. Am. Chem. Soc.*, 2014, **136**, 3334–3337.
112 Z. Zhang, H. Zhao, H. Kojima, T. Mori and K. R. Dunbar, *Chem.–Eur. J.*, 2013, **19**, 3348–3357.
113 I. Hod, M. D. Sampson, P. Deria, C. P. Kubiak, O. K. Farha and J. T. Hupp, *ACS Catal.*, 2015, **5**, 6302–6309.
114 S. Øien, G. Agostini, S. Svelle, E. Borfecchia, K. A. Lomachenko, L. Mino, E. Gallo, S. Bordiga, U. Olsbye, K. P. Lillerud and C. Lamberti, *Chem. Mater.*, 2015, **27**, 1042–1056.
115 S. Guha, F. S. Goodson, L. J. Corson and S. Saha, *J. Am. Chem. Soc.*, 2012, **134**, 13679–13691.
116 S. V. Bhosale, C. H. Jani and S. J. Langford, *Chem. Soc. Rev.*, 2008, **37**, 331–342.
117 S.-L. Suraru and F. Würthner, *Angew. Chem., Int. Ed.*, 2014, **53**, 7428–7448.
118 A. Mallick, B. Garai, M. A. Addicoat, P. St. Petkov, T. Heine and R. Banerjee, *Chem. Sci.*, 2015, **6**, 1420–1425.
119 O. Shekhah, J. Liu, R. A. Fischer and C. Wöll, *Chem. Soc. Rev.*, 2011, **40**, 1081.
120 C. W. Kung, T. C. Wang, J. E. Mondloch, D. Fairen-Jimenez, D. M. Gardner, W. Bury, J. M. Klingsporn, J. C. Barnes, R. Van Duyne, J. F. Stoddart, M. R. Wasielewski, O. K. Farha and J. T. Hupp, *Chem. Mater.*, 2013, **25**, 5012–5017.
121 B. Garai, A. Mallick and R. Banerjee, *Chem. Sci.*, 2016, **7**, 2195–2200.
122 C. F. Leong, T. B. Faust, P. Turner, P. M. Usov, C. J. Kepert, R. Babarao, A. W. Thornton and D. M. D'Alessandro, *Dalton Trans.*, 2013, **42**, 9831.
123 B. Tian, G. H. Ning, Q. Gao, L. M. Tan, W. Tang, Z. Chen, C. Su and K. P. Loh, *ACS Appl. Mater. Interfaces*, 2016, **8**, 31067–31075.
124 K. AlKaabi, C. R. Wade and M. Dincă, *Chem*, 2016, **1**, 264–272.
125 C. Lambert and G. Nöll, *J. Am. Chem. Soc.*, 1999, **121**, 8434–8442.
126 S. Amthor, B. Noller and C. Lambert, *Chem. Phys.*, 2005, **316**, 141–152.
127 Y. E. Cheon and M. P. Suh, *Angew. Chem., Int. Ed.*, 2009, **48**, 2899–2903.
128 C. Hua, A. Baldansuren, F. Tuna, D. Collison and D. M. D'Alessandro, *Inorg. Chem.*, 2016, **55**, 7270–7280.
129 J. Ferraris, D. O. Cowan, V. Walatka and J. H. Perlstein, *J. Am. Chem. Soc.*, 1973, **95**, 948–949.
130 M. Bendikov, F. Wudl and D. F. Perepichka, *Chem. Rev.*, 2004, **104**, 4891–4946.
131 Y. R. Qin, Q. Y. Zhu, L. Bin Huo, Z. Shi, G. Q. Bian and J. Dai, *Inorg. Chem.*, 2010, **49**, 7372–7381.
132 T. Chen, P. Huo, J.-L. Hou, J. Xu, Q.-Y. Zhu and J. Dai, *Inorg. Chem.*, 2016, **55**, 12758–12765.
133 H. Y. Wang, J. Y. Ge, C. Hua, C. Q. Jiao, Y. Wu, C. F. Leong, D. M. D'Alessandro, T. Liu and J. L. Zuo, *Angew. Chem., Int. Ed.*, 2017, **56**, 5465–5470.
134 J. Su, S. Yuan, H.-Y. Wang, L. Huang, J.-Y. Ge, E. Joseph, J. Qin, T. Cagin, J.-L. Zuo and H.-C. Zhou, *Nat. Commun.*, 2017, **8**, 2008.
135 *IUPAC. Compendium of Chemical Terminology (the 'Gold Book')*, ed. A. D. McNaught and A. Wilkinson, Blackwell Scientific Publications, Oxford, 2nd edn, 1997.
136 J. Roncali, *Chem. Rev.*, 1992, **92**, 711–738.
137 B. Gui, X. Meng, Y. Chen, J. Tian, G. Liu, C. Shen, M. Zeller, D. Yuan and C. Wang, *Chem. Mater.*, 2015, **27**, 6426–6431.
138 J. A. DeGayner, I. R. Jeon, L. Sun, M. Dincă and T. D. Harris, *J. Am. Chem. Soc.*, 2017, **139**, 4175–4184.
139 C. A. Fernandez, P. C. Martin, T. Schaef, M. E. Bowden, P. K. Thallapally, L. Dang, W. Xu, X. Chen and B. P. McGrail, *Sci. Rep.*, 2015, **4**, 6114.
140 A. López-Moreno, D. Clemente-Tejeda, J. Calbo, A. Naeimi, F. A. Bermejo, E. Ortí and E. M. Pérez, *Chem. Commun.*, 2014, **50**, 9372–9375.
141 T. I. Mangnall, PhD thesis, University of Liverpool, 2016.
142 S. Bandyopadhyay, C. Singh, P. Jash, M. W. Hussain, A. Paul and A. Patra, *Chem. Commun.*, 2018, **54**, 6796–6799.
143 J. Huang, Y. Li, R.-K. Huang, C.-T. He, L. Gong, Q. Hu, L. Wang, Y.-T. Xu, X.-Y. Tian, S.-Y. Liu, Z.-M. Ye, F. Wang, D.-D. Zhou, W.-X. Zhang and J.-P. Zhang, *Angew. Chem., Int. Ed.*, 2018, **57**, 4632–4636.
144 S. J. Garibay, J. R. Stork and S. M. Cohen, in *Progress in Inorganic Chemistry*, ed. K. D. Karlin, John Wiley & Sons, Inc., New Jersey, 2009, vol. 56, ch. 4, pp. 335–378.
145 R. J. P. Williams, *Chem. Rev.*, 1956, **56**, 299–328.
146 K. M. Kadish and E. Van Caemelbecke, in *Encyclopedia of Electrochemistry*, Wiley-VCH Verlag GmbH & Co. KGaA, Weinheim, Germany, 2007.
147 O. K. Farha, A. M. Shultz, A. A. Sarjeant, S. T. Nguyen and J. T. Hupp, *J. Am. Chem. Soc.*, 2011, **133**, 5652–5655.

148 L. Meng, Q. Cheng, C. Kim, W.-Y. Gao, L. Wojtas, Y.-S. Chen, M. J. Zaworotko, X. P. Zhang and S. Ma, *Angew. Chem., Int. Ed.*, 2012, **51**, 10082–10085.
149 A. Fateeva, P. A. Chater, C. P. Ireland, A. A. Tahir, Y. Z. Khimyak, P. V. Wiper, J. R. Darwent and M. J. Rosseinsky, *Angew. Chem., Int. Ed.*, 2012, **51**, 7440–7444.
150 H.-J. Son, S. Jin, S. Patwardhan, S. J. Wezenberg, N. C. Jeong, M. So, C. E. Wilmer, A. A. Sarjeant, G. C. Schatz, R. Q. Snurr, O. K. Farha, G. P. Wiederrecht and J. T. Hupp, *J. Am. Chem. Soc.*, 2013, **135**, 862–869.
151 H. Nagatomi, N. Yanai, T. Yamada, K. Shiraishi and N. Kimizuka, *Chem.–Eur. J.*, 2018, **24**, 1806–1810.
152 C. W. Kung, T. H. Chang, L. Y. Chou, J. T. Hupp, O. K. Farha and K. C. Ho, *Electrochem. Commun.*, 2015, **58**, 51–56.
153 C.-W. Kung, T.-H. Chang, L.-Y. Chou, J. T. Hupp, O. K. Farha and K.-C. Ho, *Chem. Commun.*, 2015, **51**, 2414–2417.
154 M. Lions, J.-B. Tommasino, R. Chattot, B. Abeykoon, N. Guillou, T. Devic, A. Demessence, L. Cardenas, F. Maillard and A. Fateeva, *Chem. Commun.*, 2017, **53**, 6496–6499.
155 L. Braglia, E. Borfecchia, K. A. Lomachenko, A. L. Bugaev, A. A. Guda, A. V. Soldatov, B. T. L. Bleken, S. Øien-Ødegaard, U. Olsbye, K. P. Lillerud, S. Bordiga, G. Agostini, M. Manzoli and C. Lamberti, *Faraday Discuss.*, 2017, **201**, 265–286.
156 L. Braglia, E. Borfecchia, L. Maddalena, S. Øien, K. A. Lomachenko, A. L. Bugaev, S. Bordiga, A. V. Soldatov, K. P. Lillerud and C. Lamberti, *Catal. Today*, 2017, **283**, 89–103.
157 C. Wang, Z. Xie, K. E. Dekrafft and W. Lin, *J. Am. Chem. Soc.*, 2011, **133**, 13445–13454.
158 C. Wang, J. L. Wang and W. Lin, *J. Am. Chem. Soc.*, 2012, **134**, 19895–19908.
159 S. Lin, A. K. Ravari, J. Zhu, P. M. Usov, M. Cai, S. R. Ahrenholtz, Y. Pushkar and A. J. Morris, *ChemSusChem*, 2018, **11**, 464–471.
160 X. Li, R. Van Zeeland, R. V. Maligal-Ganesh, Y. Pei, G. Power, L. Stanley and W. Huang, *ACS Catal.*, 2016, **6**, 6324–6328.
161 X. Zhang, N. A. Vermeulen, Z. Huang, Y. Cui, J. Liu, M. D. Krzyaniak, Z. Li, H. Noh, M. R. Wasielewski, M. Delferro and O. K. Farha, *ACS Appl. Mater. Interfaces*, 2018, **10**, 635–641.
162 M. Meilikhov, K. Yusenko and R. A. Fischer, *Dalton Trans.*, 2010, **39**, 10990.
163 J. E. Halls, C. Y. Cummings, J. Ellis, L. L. Keenan, D. Jiang, A. D. Burrows and F. Marken, *Mol. Cryst. Liq. Cryst.*, 2012, **554**, 12–21.
164 J. E. Halls, S. D. Ahn, D. Jiang, L. L. Keenan, A. D. Burrows and F. Marken, *J. Electroanal. Chem.*, 2013, **689**, 168–175.
165 X.-S. Xing, Z.-W. Chen, L.-Z. Cai, C. Sun, L.-R. Cai, M.-S. Wang and G.-C. Guo, *RSC Adv.*, 2016, **6**, 24190–24194.
166 H. Fukunaga, M. Tonouchi, K. Taniguchi, W. Kosaka, S. Kimura and H. Miyasaka, *Chem.–Eur. J.*, 2018, **24**, 4294–4303.
167 Q. Chen, J. Sun, P. Li, I. Hod, P. Z. Moghadam, Z. S. Kean, R. Q. Snurr, J. T. Hupp, O. K. Farha and J. F. Stoddart, *J. Am. Chem. Soc.*, 2016, **138**, 14242–14245.
168 Y. Wang, Y. Zhang, C. Hou and M. Liu, *RSC Adv.*, 2015, **5**, 98260–98268.
169 J.-D. Xiao, Q. Shang, Y. Xiong, Q. Zhang, Y. Luo, S.-H. Yu and H.-L. Jiang, *Angew. Chem., Int. Ed.*, 2016, **55**, 9389–9393.
170 Y.-Z. Chen, Y.-X. Zhou, H. Wang, J. Lu, T. Uchida, Q. Xu, S.-H. Yu and H.-L. Jiang, *ACS Catal.*, 2015, **5**, 2062–2069.
171 M. Meilikhov, K. Yusenko and R. A. Fischer, *J. Am. Chem. Soc.*, 2009, **53**, 9644–9645.
172 J. E. Halls, A. Hernán-Gómez, A. D. Burrows and F. Marken, *Dalton Trans.*, 2012, **41**, 1475–1480.
173 S. Patwardhan and G. C. Schatz, *J. Phys. Chem. C*, 2015, **119**, 24238–24247.
174 F.-Y. Yi, R. Zhang, H. Wang, L.-F. Chen, L. Han, H.-L. Jiang and Q. Xu, *Small Methods*, 2017, **1**, 1700187.
175 S. Kempahanumakkagari, K. Vellingiri, A. Deep, E. E. Kwon, N. Bolan and K.-H. Kim, *Coord. Chem. Rev.*, 2018, **357**, 105–129.
176 P. Falcaro, R. Ricco, A. Yazdi, I. Imaz, S. Furukawa, D. Maspoch, R. Ameloot, J. D. Evans and C. J. Doonan, *Coord. Chem. Rev.*, 2016, **307**, 237–254.
177 X. Zhang, M. R. Saber, A. P. Prosvirin, J. H. Reibenspies, L. Sun, M. Ballesteros-Rivas, H. Zhao and K. R. Dunbar, *Inorg. Chem. Front.*, 2015, **2**, 904–911.
178 Z. Guo, D. K. Panda, K. Maity, D. Lindsey, T. G. Parker, T. E. Albrecht-Schmitt, J. L. Barreda-Esparza, P. Xiong, W. Zhou and S. Saha, *J. Mater. Chem. C*, 2016, **4**, 894–899.
179 P. R. McGonigal, P. Deria, I. Hod, P. Z. Moghadam, A.-J. Avestro, N. E. Horwitz, I. C. Gibbs-Hall, A. K. Blackburn, D. Chen, Y. Y. Botros, M. R. Wasielewski, R. Q. Snurr, J. T. Hupp, O. K. Farha and J. F. Stoddart, *Proc. Natl. Acad. Sci. U. S. A.*, 2015, **112**, 11161–11168.
180 Q. Yang, Q. Xu and H.-L. Jiang, *Chem. Soc. Rev.*, 2017, **46**, 4774–4808.
181 Z. Peng, Z. Jiang, X. Huang and Y. Li, *RSC Adv.*, 2016, **6**, 13742–13748.
182 T. Yang, H. Yang, S. J. Zhen and C. Z. Huang, *ACS Appl. Mater. Interfaces*, 2015, **7**, 1586–1594.
183 J. Yang, L. Yang, H. Ye, F. Zhao and B. Zeng, *Electrochim. Acta*, 2016, **219**, 647–654.
184 Y.-Z. Chen, Q. Xu, S.-H. Yu and H.-L. Jiang, *Small*, 2015, **11**, 71–76.
185 L. Shi, X. Zhu, T. Liu, H. Zhao and M. Lan, *Sens. Actuators, B*, 2016, **227**, 583–590.
186 J. Yang, H. Ye, F. Zhao and B. Zeng, *ACS Appl. Mater. Interfaces*, 2016, **8**, 20407–20414.
187 C. J. Stephenson, J. T. Hupp and O. K. Farha, *Inorg. Chem.*, 2016, **55**, 1361–1363.
188 S. Aguado, S. El-Jamal, F. Meunier, J. Canivet and D. Farrusseng, *Chem. Commun.*, 2016, **52**, 7161–7163.
189 Y.-Z. Chen, Z. U. Wang, H. Wang, J. Lu, S.-H. Yu and H.-L. Jiang, *J. Am. Chem. Soc.*, 2017, **139**, 2035–2044.
190 D. M. D'Alessandro, J. R. R. Kanga and J. S. Caddy, *Aust. J. Chem.*, 2011, **64**, 718.

191 T. B. Faust and D. M. D'Alessandro, *RSC Adv.*, 2014, **4**, 17498–17512.
192 H. Miyasaka, *Acc. Chem. Res.*, 2013, **46**, 248–257.
193 J. B. Torrance, J. E. Vazquez, J. J. Mayerle and V. Y. Lee, *Phys. Rev. Lett.*, 1981, **46**, 253–257.
194 J. B. Torrance, *Mol. Cryst. Liq. Cryst.*, 1985, **126**, 55–67.
195 H. Miyasaka, C. S. Campos-Fernández, R. Clérac and K. R. Dunbar, *Angew. Chem.*, 2000, **112**, 3989–3993.
196 H. Miyasaka, N. Motokawa, S. Matsunaga, M. Yamashita, K. Sugimoto, T. Mori, N. Toyota and K. R. Dunbar, *J. Am. Chem. Soc.*, 2010, **132**, 1532–1544.
197 H. Miyasaka, T. Izawa, N. Takahashi, M. Yamashita and D. R. Kim, *J. Am. Chem. Soc.*, 2006, **128**, 11358–11359.
198 C. F. Leong, P. M. Usov and D. M. D'Alessandro, *MRS Bull.*, 2016, **41**, 858–864.
199 K. Taniguchi, K. Narushima, J. Mahin, W. Kosaka and H. Miyasaka, *Angew. Chem., Int. Ed.*, 2016, **55**, 5238–5242.
200 K. Taniguchi, K. Narushima, H. Sagayama, W. Kosaka, N. Shito and H. Miyasaka, *Adv. Funct. Mater.*, 2017, **27**, 1–10.
201 T. L. Easun, J. Jia, T. J. Reade, X.-Z. Sun, E. S. Davies, A. J. Blake, M. W. George and N. R. Champness, *Chem. Sci.*, 2014, **5**, 539–544.
202 M. D. Allendorf, M. E. Foster, F. Léonard, V. Stavila, P. L. Feng, F. P. Doty, K. Leong, E. Y. Ma, S. R. Johnston and A. A. Talin, *J. Phys. Chem. Lett.*, 2015, **6**, 1182–1195.
203 C. H. Hendon and A. Walsh, *Chem. Sci.*, 2015, **6**, 3674–3683.
204 J.-J. Liu, Y.-F. Guan, L. Li, Y. Chen, W.-X. Dai, C.-C. Huang and M.-J. Lin, *Chem. Commun.*, 2017, **53**, 4481–4484.
205 S. Takaishi, M. Hosoda, T. Kajiwara, H. Miyasaka, M. Yamashita, Y. Nakanishi, Y. Kitagawa, K. Yamaguchi, A. Kobayashi and H. Kitagawa, *Inorg. Chem.*, 2009, **48**, 9048–9050.
206 Y. Kobayashi, B. Jacobs, M. D. Allendorf and J. R. Long, *Chem. Mater.*, 2010, **22**, 4120–4122.
207 L. Sun, C. H. Hendon, M. A. Minier, A. Walsh and M. Dincă, *J. Am. Chem. Soc.*, 2015, **137**, 6164–6167.
208 M. L. Aubrey, B. M. Wiers, S. C. Andrews, T. Sakurai, S. E. Reyes-Lillo, S. M. Hamed, C.-J. Yu, L. E. Darago, J. A. Mason, J.-O. Baeg, F. Grandjean, G. J. Long, S. Seki, J. B. Neaton, P. Yang and J. R. Long, *Nat. Mater.*, 2018, **17**, 625–632.
209 D. Bradshaw, A. Garai and J. Huo, *Chem. Soc. Rev.*, 2012, **41**, 2344–2381.
210 X. Nie, A. Kulkarni and D. S. Sholl, *J. Phys. Chem. Lett.*, 2015, **6**, 1586–1591.
211 W.-X. Zhang, P.-Q. Liao, R.-B. Lin, Y.-S. Wei, M.-H. Zeng and X.-M. Chen, *Coord. Chem. Rev.*, 2015, **293–294**, 263–278.
212 Q. Li, W. Zhang, O. Š. Miljanić, C. B. Knobler, J. F. Stoddart and O. M. Yaghi, *Chem. Commun.*, 2010, **46**, 380–382.
213 M. B. Robin and P. Day, *Adv. Inorg. Chem. Radiochem.*, 1968, **10**, 247–422.
214 K. Otsubo, Y. Wakabayashi, J. Ohara, S. Yamamoto, H. Matsuzaki, H. Okamoto, K. Nitta, T. Uruga and H. Kitagawa, *Nat. Mater.*, 2011, **10**, 291–295.
215 H. J. Buser, D. Schwarzenbach, W. Petter and A. Ludi, *Inorg. Chem.*, 1977, **16**, 2704–2710.
216 J. N. Behera, D. M. D'Alessandro, N. Soheilnia and J. R. Long, *Chem. Mater.*, 2009, **21**, 1922–1926.
217 G. Férey, F. Millange, M. Morcrette, C. Serre, M. L. Doublet, J. M. Grenèche and J. M. Tarascon, *Angew. Chem., Int. Ed.*, 2007, **46**, 3259–3263.
218 J. W. Yoon, Y. K. Seo, Y. K. Hwang, J. S. Chang, H. Leclerc, S. Wuttke, P. Bazin, A. Vimont, M. Daturi, E. Bloch, P. L. Llewellyn, C. Serre, P. Horcajada, J. M. Grenèche, A. E. Rodrigues and G. Férey, *Angew. Chem., Int. Ed.*, 2010, **49**, 5949–5952.
219 Q. Sun, M. Liu, K. Li, Y. Han, Y. Zuo, J. Wang, C. Song, G. Zhang and X. Guo, *Dalton Trans.*, 2016, **45**, 7952–7959.
220 S. Benmansour, A. Abhervé, P. Gómez-Claramunt, C. Vallés-García and C. J. Gómez-García, *ACS Appl. Mater. Interfaces*, 2017, **9**, 26210–26218.
221 L. Sun, T. Miyakai, S. Seki and M. Dincă, *J. Am. Chem. Soc.*, 2013, **135**, 8185–8188.
222 T. Okubo, N. Tanaka, K. H. Kim, H. Anma, S. Seki, A. Saeki, M. Maekawa and T. Kuroda-Sowa, *Dalton Trans.*, 2011, **40**, 2218–2224.
223 A. Ahmed, C. M. Robertson, A. Steiner, T. Whittles, A. Ho, V. Dhanak and H. Zhang, *RSC Adv.*, 2016, **6**, 8902–8905.
224 C. Jiao, X. Jiang, H. Chu, H. Jiang and L. Sun, *CrystEngComm*, 2016, **18**, 8683–8687.
225 C. Hua, A. Rawal, T. B. Faust, P. D. Southon, R. Babarao, J. M. Hook and D. M. D'Alessandro, *J. Mater. Chem. A*, 2014, **2**, 12466–12474.
226 I. R. Jeon, B. Negru, R. P. Van Duyne and T. D. Harris, *J. Am. Chem. Soc.*, 2015, **137**, 15699–15702.
227 M. E. Ziebel, L. E. Darago and J. R. Long, *J. Am. Chem. Soc.*, 2018, **140**, 3040–3051.
228 J. Calbo, J. Aragó, F. Otón, V. Lloveras, M. Mas-Torrent, J. Vidal-Gancedo, J. Veciana, C. Rovira and E. Ortí, *Chem.–Eur. J.*, 2013, **19**, 16656–16664.
229 J. Calbo, J. Aragó and E. Ortí, *Theor. Chem. Acc.*, 2013, **132**, 1330.
230 P.-T. Chiang, N.-C. Chen, C.-C. Lai and S.-H. Chiu, *Chem.–Eur. J.*, 2008, **14**, 6546–6552.
231 M. Yoshizawa, K. Kumazawa and M. Fujita, *J. Am. Chem. Soc.*, 2005, **127**, 13456–13457.
232 S.-L. Cai, Y.-B. Zhang, A. B. Pun, B. He, J. Yang, F. M. Toma, I. D. Sharp, O. M. Yaghi, J. Fan, S.-R. Zheng, W.-G. Zhang and Y. Liu, *Chem. Sci.*, 2014, **5**, 4693–4700.